LBL-7713

MASTER

STUDY OF THE ROLE OF COMPLETE FUSION IN THE REACTION OF ^{48}Ca AND ^{56}Fe WITH CERIUM AND TERBIUM

David Joseph Morrissey
(Ph. D. thesis)

May 1978

Prepared for the U. S. Department of Energy
under Contract W-7405-ENG-48

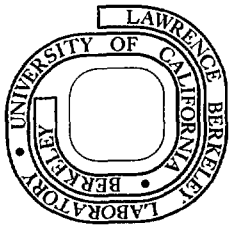

LBL-7713

TABLE OF CONTENTS

DEDICATION

I would like to dedicate this work to the many people in my life who, through my contact with them, have both enriched my life and have helped me to form a clear picture of what my life should be. These people represent a broad class too numerous to mention ranging from Warren W. Miller to Glenn T. Seaborg and from John J. King to my wife Deborah and my family.

STUDY OF THE ROLE OF COMPLETE FUSION IN THE REACTION OF ^{48}Ca AND ^{56}Fe WITH CERIUM AND TERBIUM

David Joseph Morrissey

Lawrence Berkeley Laboratory
University of California
Berkeley, CA 94720

ABSTRACT

^{48}Ca and ^{56}Fe beams from the Super HILAC accelerator were used to irradiate thick metal foils of cerium and terbium. Product gamma ray activities were detected offline and individual products were identified by half-life, gamma ray energy and gamma ray abundances. The production cross sections were iteratively fit to charge and mass dispersions to allow correction for parent decay and calculation of mass yields. From the mass yield curves contributions from quasielastic transfer, deep inelastic transfer and complete fusion reaction mechanisms were inferred. Complete fusion was made up of contributions from both evaporation residue and fusion-fission products for the ^{48}Ca induced reactions. However, only fusion-fission products were detected in the ^{56}Fe induced reactions.

Critical angular momenta for fusion were found to be 82 ± 8 h for $^{48}Ca + ^{159}Tb$ and 34 ± 5 h for $^{56}Fe + ^{140}Ce$, which can be compared with 53 ± 8 h for $^{12}C + ^{197}Au$ (Natowitz, 1970) and 86 ± 5 h for $^{40}Ar + ^{165}Ho$ (Hanappe, 1973). All of these reactions lead to essentially the same compound nucleus and seem to show the dramatic decline in complete fusion for heavy ions larger than ^{40}Ar. The prediction of this decline was found to be beyond the model calculations of Bass and the critical distance approach of Glas and Mosel.

ACKNOWLEDGMENTS

It is my pleasure to acknowledge the assistance of all those who have contributed to my completion of this work. I wish to thank Glenn T. Seaborg who took me on as a graduate student and as my research director gave me both the latitude and support to participate in many areas of nuclear science research in a meaningful way.

Thanks are due to Walter D. Loveland on whose advice and example I have relied since our first meeting during his sabbatical visit to Berkeley.

Thanks are also due to Roland J. Otto and Diana Lee who have been at the heart of the Seaborg research group for the past several years where they laid the ground work and fostered the development of the methods that I used in this study.

Special thanks are due to my wife, Deborah, who has encouraged me throughout.

This work has been supported by the U.S. Department of Energy.

I. INTRODUCTION

A. Background

In recent years the field of nuclear science has been dominated by research with heavy ion projectiles. The term heavy ion has rather loosely been associated with projectiles larger than ^{4}He or alpha particles, but its meaning and usage has generally followed the evolution of the capability of the accelerators that produced these ion beams. As the contemporary accelerators have the capability of accelerating any ion, from $^{1}_{1}H$ to $^{238}_{92}U$, qualified loosely defined descriptions such as light-heavy ion[1] and very-heavy ion[2,3] have appeared in the literature. A primary moving force behind heavy ion nuclear science in the past has been the systematic extension of the naturally occurring period table to new elements through heavy ion reactions on heavy element targets. Notable success in this effort was seen in the synthesis of elements through $Z = 106$ by complete fusion reactions of light heavy ions, $Z \lesssim 10$, with targets such as ^{249}Cf.[4] In these reactions only two mechanisms were thought to be operating, compound nucleus formation or complete fusion, followed by deexcitation of the statistically equilibrated compound nucleus,[5] and direct reactions. This deexcitation of the compound nuclei came to favor the binary fission mode more and more as the Z of the compound nucleus was pushed further and further beyond the limits of the known nuclei. Thus, the situation appeared that for projectiles up to ^{40}Ar the limit on production of new elements was assumed to be on binary fission deexcitation of the compound nuclei.[6]

However, a break seemed to occur with the next heaviest projectile studied, ^{84}Kr. In the earliest studies of the interactions of ^{84}Kr projectiles with heavy element targets, such as ^{209}Bi[7,8] and ^{238}U,[9] only a very small percentage of the observed reaction products could be associated with the complete fusion-fission reaction mechanism. In fact a new reaction mechanism was found to be operating in these very-heavy ion induced nuclear reactions, which was termed a deep inelastic transfer process because the products were typically very inelastically scattered with relatively small mass exchange. (This process has been recently reviewed by Schroder and Huizenga.[10]) And as even heavier-heavy ions, such as ^{136}Xe, were accelerated and reacted with heavy element targets[11,12] no reaction products could be attributed to the complete fusion-fission of the target and projectile.

Thus, there appeared to be a large change in the role of complete fusion between heavy ion projectiles and high mass targets as one went from $^{40}_{18}Ar$ to $^{84}_{36}Kr$ induced reactions. Perhaps this is not unexpected because such a change implies a factor of two change in the charge and mass of the projectile. And with a heavy element target such as ^{238}U the compound nucleus moves from just slightly beyond known nuclei, $Z \approx 110$, to a region beyond most theoretical predictions, $Z \approx 128$.[13] As a result of this difference, coupled with the discovery of a new reaction mechanism, most studies of heavy ion reactions turned toward understanding the deep inelastic reaction.[14,15,10] Because of this shift of emphasis relatively few studies of the rate of change of the role of complete fusion with heavy ion projectiles have been made. Two exceptions are the study of ^{56}Fe with ^{238}U[16] and the study of the

reaction of ^{63}Cu with various targets.[17] The reaction of ^{56}Fe with ^{238}U was very similar to previous radioanalytic studies of heavy ion induced reactions on uranium targets of the Berkeley group.[9,11,18] Comparison of the Berkeley studies with that of Reus et al.[16] showed that the decline of the complete fusion cross section with projectile's Z was rather steep. The contribution of complete fusion to the total reaction cross section dropped from ~55% (^{40}Ar), to ~14% (^{56}Fe), to ~4% (^{84}Kr). This qualitative comparison is reasonable because these three studies were carried out in a similar fashion and at similar values of the parameter $\bar{E}/B$, the average bombarding energy ($\bar{E}$) divided by the coulomb potential at the interaction radius ($B = V_{coul}(R_{INT})$). This parameter has been suggested as the basis for an empirical scaling law for the characteristic features of heavy ion induced deep inelastic reactions by Mathews et al.[19] Again, this comparison suffers from the problem that the compound nuclei $^{278}110$, $^{294}118$, and $^{322}128$ are all unknown and that the complete fusion cross section falls with the removal of the compound system from known nuclei.

This situation is very different from that observed for light heavy ions incident on low and medium mass targets where the complete fusion cross section represented nearly the entire reaction cross section.[20-23] And also it is different from reactions like $^{40}Ar + ^{109}Ag \rightarrow (^{149}Tb)^*$ and $^{84}Kr + ^{65}Cr \rightarrow (^{149}Tb)^*$, studied by Britt et al., because the complete fusion cross section was found to be greater than one half of the reaction cross section.[24] And even for the case of ^{84}Kr plus ^{165}Ho Peter et al. found that ~25% of the reaction cross section could be attributed to complete fusion.[25] Thus the qualitative picture that

emerges is that the amount of complete fusion in a given reaction decreases sharply when the projectile is more massive than ^{40}Ar, unless the compound system is within the bounds of "known nuclei". However, data for projectiles heavier than ^{40}Ar are limited to a few studies of ^{56}Fe and ^{63}Cu and ^{84}Kr.[16,17,9,24,25]

B. Proposed Study

1. Projectile-Target Combinations

In this study I have explored the role of complete fusion in the reaction of ^{48}Ca and ^{56}Fe projectiles with cerium and terbium targets. The choice of projectiles is based on the need for study of systems in the transition region between ^{40}Ar and ^{84}Kr over which the role of the complete fusion process has been shown to change dramatically.[2] Also, studies with ^{32}S,[20,21] ^{35}Cl[22,26] and ^{56}Fe[16] indicate that the transition occurs rather sharply in the ^{40}Ar region. The reason for the choice of rare earth element targets is twofold: the compound systems for the four projectile-target combinations are well within the bounds of "known nuclei";[27] and secondly that the reaction of ^{48}Ca with ^{159}Tb leads to very nearly the same compound system as ^{56}Fe with ^{140}Ce and also the $^{40}Ar + ^{165}Ho$ system previously studied by Tamain et al.[28] Another consideration in the selection of target nuclei is its isotopic composition. Terbium (element 65) has only one stable isotope, A = 159. However, cerium (element 58) has four naturally occurring stable isotopes. The isotopic abundances are given in Table I.[29] One can see that cerium is essentially monoisotopic with A = 140.

Table I. Natural Abundances of Cerium Isotopes*

Mass Number	136	138	140	142
Percent Natural Abundance	0.193	0.250	88.48	11.07

*from G.L. Trigg, Reference 29

The projectile-target combinations and the nominal compound nuclei are listed in Table II. With the exception of ^{215}Pa the compound nuclei are known.[27] Also shown in Table II are the reaction Q values for the four systems studied,[30,31] with the assumption that natural cerium $\approx ^{140}Ce$. The Q values gradually become more negative in value as the compound nucleus mass increases. This will work to offset the increase in the reaction coulomb barrier with the Z_1Z_2 product to give similar excitation energies of the compound nuclei (see below).

Table II. Compound Nuclei and Reaction Q Values

Projectile	Target	Compound nucleus	Reaction* Q value (MeV)
$^{48}_{20}Ca$	$^{140}_{58}Ce$ ($^{Nat}_{58}Ce$)	$^{188}_{78}Pt$	- 94.7
$^{48}_{20}Ca$	$^{159}_{65}Tb$	$^{207}_{85}At$	-100.4
$^{56}_{26}Fe$	$^{140}_{58}Ce$ ($^{Nat}_{58}Ce$)	$^{196}_{84}Po$	-136.0**
$^{56}_{26}Fe$	$^{159}_{65}Tb$	$^{215}_{91}Pa$	-146.9**

* Masses from A.H. Wapstra and K. Bos, Reference 30

**Masses from W.D. Myers, Reference 31

There is, however, one rather large difference between ^{140}Ce and ^{159}Tb. The lighter target, ^{140}Ce, has 82 neutrons (a magic number)

and is thought to be spherical. This is supported by its low value of $\beta/\beta_{sp} \cong 4$,[32] the ratio of the measured quadrupole deformation parameter to the single particle model quadrupole deformation parameter. This deformation parameter is proportional to the difference between the extension of the nucleus along the body symmetry axis and an axis perpendicular to it. However, $\beta/\beta_{sp} \cong 15$ for ^{159}Tb, a value which is among the largest for non-actinide elements.[32] Rasmussen and Sugawara-Tanabe[33] have treated nuclear reactions on deformed nuclei and draw the conclusion that "at higher bombarding energies the reaction cross section for deformed nuclei should be asymptotic with the classical formula for spheres." Wong[34] also developed a series of mathematical expressions to describe the cross section for interactions with deformed targets which led to the same conclusion that deformation effects are only important near the interaction barrier. Thus, the large difference in the shapes of the two target nuclei should not affect the overall features of the reaction due to the high bombarding energy used (see below), but any effect on the relative population of the various reaction channels remains to be determined.

2. Methodology

In order to properly measure the fraction of the total reaction cross section that goes into complete fusion one must choose a method that is simultaneously sensitive to all reaction channels, or perform several studies each focusing on a specific reaction channel which will be meshed together later to give the overall picture. Previously reported studies of complete fusion have ranged from mica track detector[35]

and gasjet recoil collection measurements of only the evaporation residues,[36] to counter telescope measurements of correlated fission fragments[6,26] or evaporation residues[22], to radiochemical measurement of the radioactive reaction products.[18,37] Of these the mica track detector method will not work with ^{48}Ca and ^{56}Fe projectiles because the mica would be nearly as sensitive to the projectiles as to the reaction products.[38] Also, the survival of evaporation residue products decreases sharply in the region of the compound nuclei of this study and therefore constitute a smaller and smaller fraction of the complete fusion cross section.

Of the remaining methods the radiochemical or radio-analytical method has several attractive features: it is very efficient in terms of accelerator utilization, typical irradiations of target materials are on the order of hours, and, barring systematically peculiar radioactive decay of specific product nuclei, is simultaneously sensitive to all the reaction channels. However, it must be noted that all kinematic information is lost in the radiochemical studies. This has been shown to be very important in determining the division of the reaction cross section between reaction channels or mechanisms that lead to "similar" radioactive products.[2] In particular, the distinction between quasielastic and deep inelastic products is based on the kinematic difference of the amount of energy dissipated in the reaction that formed the products and so discrepancies between counter-telescope[8,39] and radiochemical studies[9] have appeared.[2]

And so with this caution, the radioanalytical survey of induced radioactivities was used to study the role of complete fusion products

from the interaction of ^{48}Ca and ^{56}Fe ions with cerium and terbium targets.

II. EXPERIMENTAL METHOD

The radioanalytical method for the study of heavy ion reactions has been developed in several laboratories around the world[16,18,40] and particularly in Berkeley by the Seaborg group.[9,11,18,41,42] The method has been recently described in detail[42-44] by the Berkeley group. Generally, the measurement involves the irradiation of an infinitely thick target of a pure element, meaning the incident ions are stopped in the target. Therefore target nuclei interact with beam particles with energies ranging from the incident energy down to the interaction barrier (the implications of this will be described later). Subsequent to irradiation the radioactivities are surveyed with a gamma-ray spectrometer and products identified via their characteristic gamma-ray energies and half lives.

Once a set of measured product yields has been generated these yields are fit to charge dispersion curves with an iterated procedure to correct for parent beta (and alpha, when possible) decay feeding, because, as in fission studies, radiochemical product yield measurements fall into two categories, cumulative and independent yields,[45] where cumulative indicates that the measured product yield has summed some fraction of its beta decay isobaric chain. The term independent indicates that there has been no feeding by radioactive decay to that product. Thus, using the independent yields as guides, one can construct post-neutron and charged particle evaporation, pre-beta decay, mass and charge distribution curves for the nuclear reaction.

A. Irradiations

All the irradiations were performed at the Super HILAC at the Lawrence Berkeley Laboratory; a linear accelerator capable of accelerating heavy ion beams up to energies of 8.5 MeV/nucleon.[46] The irradiations with ^{56}Fe projectiles were performed in the "straight through" beam line E2. Sequential irradiation of the cerium and terbium targets was performed with a 473 ± 14 (FWHM) MeV ^{56}Fe beam. The energy of the projectiles was monitored by periodically inserting a thin gold foil (~200 μg/cm^2) on an aluminum support (~230 μg/cm^2) and measuring the elastically scattered ^{56}Fe projectiles at 16° to the beam with a Si-Au surface barrier detector.[47] Irradiation of the cerium lasted 105 minutes with an average beam intensity of 5.1 x 10^{12} particles/minute, and irradiation of the terbium was for 137 minutes at an average flux of 1.5 x 10^{13} particles/minute.

The ^{48}Ca bombardments were performed in the magnetically analyzed E53 beam line as part of a series of experiments using this exotic projectile.[47-50] In fact this series of experiments was the first to make use of the newly developed ^{48}Ca beam at the Super HILAC.[51] The beam energy was measured by attenuating the beam and using an in-line Si-Au surface barrier detector; the energy was found to be 405 ± 12 (FWHM) MeV. The cerium and terbium targets were irradiated simultaneously with a ^{208}Pb target,[48] by using the rare earth elements as beam defining collimators. This was not the most preferable situation but the high cost and low availability of ^{48}Ca beams necessitated it. As a result the actual beam flux was not measured but was estimated to be ~1 x 10^{12} particles/minute lasting for 269 minutes. The estimation

of the beam flux on the collimator was taken to be the difference of the entire beam measured at an upstream position minus that which went through the collimator annd hit the ^{208}pb target. This was not a serious problem because (a) we were concerned with measuring the fraction of the total reaction cross section that goes into complete fusion, and (b) the cross sections could be extracted from calculations based on previously developed systematics of the total reaction cross sections for heavy ion reactions[10] (see below).

B. Targetry

Target foils 2[illegible] x 25 x 0.25 mm supplied by Alfa-Venton Corporation, Danvers, Massachusetts, were used in the ^{48}Ca bombardments. Specifications for the cerium and terbium foils called for 99.9 percent purity. However, subsequent to bombardment the foils were surveyed by L X-ray fluorescence spectroscopy for impurities. This analysis showed that the terbium foil contained ~0.5 percent cerium.[52] This level of contamination was not serious but was observable (see below) in the reaction products. Target foils with the same specifications were subsequently obtained from Research Chemicals, Phoenix, Arizona. These foils were found to meet the specifications.

The targets were supported in the beam path in vacuum by a specifically designed holder.[53] The holder consisted of a water cooled beam collimator and a retractable target support and vacuum lock. These features allowed rapid removal of the target materials from the beam line subsequent to bombardment. Target foils were clamped in the support and low conductivity water was sprayed in a jet up against the back

face of the target foil by a recirculating pump. The beam flux was integrated by a Brookhaven Instruments Corporation electrometer and spurious beam readings were suppressed by an ~500 gauss magnetic field at the target.

Cerium is air sensitive in the metal form, readily oxidizing on all exposed surfaces, which leads to flaking. Therefore the cerium foils used in the bombardments were stored in an oil bath until just prior to irradiation, when they were washed with acetone to remove the oil. Terbium foils are not air sensitive so the oil bath was not used. However, each foil was rinsed with acetone to remove surface contaminants prior to bombardment.

C. Gamma-Ray Spectroscopy

All gamma-ray spectrometric measurements were made with an ORTEC coaxial-germanium diode with drifted lithium compensation, this detector had a nominal 60 cm^3 active volume. The samples were mounted on 8.8 x 6.3 x 0.16 cm aluminum cards which were held rigidly in a lucite holder attached to the Ge(Li) detector. This holder was machined to reproducibly hold the sample cards in approximately 14 known geometries relative to the detector. The detector, sample and lucite sample rack were contained in a graded shield of volume ~1 m^3 to reduce contributions from ambient background. The shield contained 5 cm of lead, 0.3 cm steel and 0.3 cm aluminum.

Signals arising in the Ge(Li) detector, were fed into an ORTEC charge sensitive preamp and then into a high rate amplifier which had been matched to the input specifications of a 50 megahertz Northern Scientific

ADC. This ADC was part of a pulse height analysis system that included a Texas Instruments TI-960A minicomputer and an Ampex magnetic tape drive. This system was programmed to collect a single 4096 channel spectrum along with a 40 character identifier and output this information with the data onto magnetic tape.[54] A real time clock with a Julian calendar was added to enable the system to record the real time start and stop points of each measurement on the magnetic tape with each spectrum.

1. Energy Calibration of System

All calibrations of the systems were performed with a National Bureau of Standards standard reference material gamma-ray source, SRM-4216-C. This is a mixed radionuclide, essentially windowless, point source that can be used for energy as well as for efficiency calibration of high resolution gamma ray detectors. A list of the radiations from the nuclides present in the standard used in the energy calibration of the Ge(Li) detector is given in Table III. The exact energy calibration was made by fitting the centroids of the known energy gamma-ray peaks as determined by SAMPO[55,56] (see below) to a third order polynomial of the form:

$$E_\gamma = \sum_{i=1}^{4} a_i \ (\text{Channel No.})^{i-1} \qquad (1)$$

The polynomial in centroid channel number was least squares fit to the known energies of the gamma rays from the standard with the computer code ORGLS[57] as well as with a least squares routine contained in

SAMPO.[55] Typical values of the coefficients of the second and third degree polynomial terms were 5.2×10^{-7} and -3.3×10^{-11}, respectively for an energy calibration in keV.

Table III. NBS Mixed Radionuclide Emission Rate Point Source SRM-4216-C

Nuclide	E_γ (keV)	Half-life (days)	Emission Rate* (gammas/min)
^{109}Cd	88.0	464.6	24960
^{57}Co	122.1	271.4	38154
^{139}Ce	165.8	137.8	42288
^{203}Hg	279.2	46.61	88440
^{113}Sn	391.7	115.3	97500
^{85}Sr	514.0	64.86	154920
^{137}Cs	661.6	30.17**	105840
^{60}Co	1173.2	5.272**	233220
	1332.5		233520
^{88}Y	898.0	106.6	563100
	1836.1		588960

* at 1200 EST, 1 Sept. 1975
**half-life in years

The resolution of the entire spectometer system was also measured with the SRM-4216-C standard. The resolution of a Ge(Li) spectrometer is traditionally quoted in terms of the FWHM of the ^{60}Co 1332.5 keV gamma-ray peak; this value was found to be 2.1 ± .05 keV and remained constant throughout the experiments.

2. Efficiency Calibration of System

All the efficiency calibrations were performed with the NBS standard SRM-4216-C by comparing the known gamma-ray emission rates with those measured as a function of both geometry and energy. The energy dependence of the efficiency, ϵ_γ, of Ge(Li) gamma ray detectors has been postulated to have the form:[58]

$$\epsilon_\gamma(E_\gamma) = P_1 [E_\gamma^{P_2} + P_3 \exp (P_4 E_\gamma)]. \qquad (2)$$

The efficiency of the Ge(Li) spectrometer system was measured and coefficients obtained by least squares fitting equation 2 to the measured gamma-ray emission rates for all the possible geometries.

3. Measurement Strategy

The initial β-γ activity of the samples was on the order of a few tens of mr/cm^2-hr measured at a distance of approximately 0.5 meters. The samples were removed from the beam line, prepared for measurement, and transported to the gamma-ray spectrometer system in an average time of approximately 10 minutes. The gamma-ray spectrometer was located away from all the accelerators at LBL to reduce the gamma ray background. The decay of the radioactive products was typically followed for a period of 1.5 months after the end of bombardment. This allowed nuclides with half lives between ~30 minutes and a few hundred days to be observed.

The choice of the duration of each measurement of a given sample is dependent on many factors. Binder has considered these factors and has developed a criterion for scheduling samples.[44] The basis

of the schedule lies in recognizing that: (1) the activities that are observable in the gamma ray spectrum from a given sample obviously vary with time; and (2) given that all the production cross sections of observable nuclei are approximately equal (within a factor of 100) there is only a short period in which a product activity with a given half-life will be observable, which is the period during which that given radionuclide is going through its second, third and fourth half-lives. That is, a given radionuclide is usually not visible during its first half-life because it will be obscured by shorter lived activities. It is also not generally visible at times later than its fourth or fifth half-life because of the prominence of longer lived species. Thus, the first four measurements of each sample were for 10 minutes plus system dead time each and then the interval would be doubled to 20 minutes for the next four measurements and so on. In practice this was repeated until the length of the measurement was 24 hours which was the longest measurement period.

Throughout these schedules the geometry of the sample with respect to the detector was adjusted to maintain the ADC dead time $\lesssim$15%. As the samples became weaker the samples were moved to higher geometry with the limiting condition being that no sample was placed closer to the face of the Ge(Li) detector than 3 cm.

D. Nuclidic Identification

The product isotopes were identified by both known gamma-ray energy and half-life.[59,60] This was accomplished by extraction of the areas and energies of the full energy gamma-ray peaks from the spectra with the

computer code SAMPO.[55,60] Construction and least square fitting of decay curves for each observed gamma-ray were then performed. Finally the consistency of all the assignments was checked by verifying that all the known gamma-rays of each isotope were present in the correct ratios or if missing could be shown to be too low in intensity to be observed. The identification procedure was tremendously facilitated by the previous development of a decay curve construction computer code and an interactive decay curve identification code by the Berkeley group.[42,43] These codes were run on the Lawrence Berkeley Laboratory CDC computer system and once the gamma-ray spectra were recorded onto magnetic tape, the data and intermediate results resided in the magnetic tape library of the system. When the individual gamma-ray decay curves had been assigned to individual nuclei the results were output on punched cards for consistency review and production cross section calculations.

1. Use of SAMPO

All peak area fitting was done with an automatically operating version of SAMPO. This computer code takes the spectral input on magnetic tape and processes each spectrum individually to determine the energy that corresponds to the centroid as well as the area of all peaks with a peak to valley ratio above a level of ~2. The code outputs this information on magnetic tape for the half-life analysis, as well as a microfiche record of the fit obtained for each peak. SAMPO was chosen[42,43] for the peak fitting because it contained several attractive features. One very important aspect of the peak

fitting is the ability to "calibrate" the line shape of a peak generated by a gamma ray spectrometer. In SAMPO the line shape used to fit peaks contains a central Gaussian and an exponential tail joined smoothly on each side,[55,56] which can be adjusted via a least squares fitting to the exact line shape of the spectrometer. A second attractive feature of this code is that the code was developed to analyze "complex" spectra and as such has included the option of a smoothly varying polynomial-type background continuum. This type of background approximation is particularly well suited to the spectra that were analyzed. After the entire system has been calibrated for energy, efficiency and line shape and the input spectra have been screened to be sure that they contained the correct pertinent information, then the automatic SAMPO analysis was run.

2. Interactive Computer Graphical Half-life Analysis

After the SAMPO analysis is complete the next step of the analysis is to sort the observed gamma ray peak areas so that decay curves can be constructed. The code TAU1 was written to perform this sorting.[42,43] The code starts with the magnetic tape output from SAMPO and searches both on the spectrum identification tag and on gamma ray energy. Through the analysis the time sequence of the original measurement schedule is preserved. Thus the SAMPO analysis was performed in chronological order which TAU1 preserves, thereby eliminating any chronologic sorting in TAU1. The code then generates a new magnetic tape as output that contains the gamma ray intensities sorted by energy for each of the samples.

The next stage of the analysis is to bring the measured decay curves for each gamma ray together with a compilation of the known gamma-ray transitions in order to identify the radionuclides present in the sample. The computer code TAU2 which was used for this task is an interactive decay curve analysis program that presents decay curves and also the relevant data for the 20 nearest known gamma-ray transitions on a computer terminal to facilitate the identification. The code has been designed to run on the CDC-6400 machine at LBL with a Tektronix 4014 graphics terminal.[42,43] Input data for this code are the sorted gamma-ray data from TAU1 and a listing of the abridged gamma-ray table of Binder et al.,[59] both of which are stored on magnetic tape. The operator is then able to choose any single known line or combination of known lines to be fit to the measured decay curve, or arbitrary half-lives may be fit to the data. When an acceptable identification of the decay curve has been made, the graphical display is recorded on microfiche and the A_0 value along with its error, energy and radionuclide identification are output on a punched card.

3. Cross Sections

Cross sections are calculated for each component of every decay curve by using the A_0 value and half life on the punched card output from TAU2 in the well-known equation:[61]

$$\sigma = \frac{A_o}{N_t \phi \ (1 - e^{-\lambda t_B})} \qquad (3)$$

where N_t is the number of target nuclei in nuclei per square centimeter, ϕ is the beam flux in particles per minute (the flux of the ^{48}Ca and ^{56}Fe was nearly constant throughout the short irradiations used in this work), σ is the cross section in square centimeters, λ is the decay constant in reciprocal minutes and t_B the length of the bombardment in minutes.

The number of target nuclei, N_t, was calculated with the aid of the Northcliffe-Schilling range energy tables.[62] Because the targets were infinitely thick N_t can simply be calculated as the difference between the range of the incident projectile and the range of the projectile when its kinetic energy equals the interaction barrier in the laboratory system. These values, given in Table IV, are taken from Northcliffe and Schilling,[62] although some deviations from the calculated ranges have been observed.[63] Values for the range in cerium and terbium were obtained by linear interpolation between tabulated stopping media and corrections for different projectile mass number were performed as suggested.[62]

Table IV. Calculated Target Thicknesses*

Syatem	$E_{lab}^{initial}$ (MeV)	Total (mg/cm^2)	Range at $E_{lab} = B$** (mg/cm^2)	Δ (mg/cm^2)
^{48}Ca + Ce	405 ±12	51.4 ± 1.7	22.3 ± 0.1	29.1 ± 1.8
^{48}Ca + Tb	405 ± 12	55.4 ± 1.9	25.6 ± 0.1	29.8 ± 2.0
^{56}Fe + Ce	473 ± 14	43.2 ± 1.4	21.9 ± 0.2	21.9 ± 1.6
^{56}Fe + Tb	473 ± 14	46.7 ± 1.5	25.4 ± 0.2	21.3 ± 1.7

* Calculated according to Ref. 62.
**B is the laboratory interaction barrier.

It is at this point that all the assignments of the decay curves to known gamma-ray transitions were consistent and thereby correct. This is accomplished by checking each isotope to be sure that:

(a) the gamma-ray transitions were assigned to that nuclide uniquely, i.e. if multiple assignments were made to an observed gamma-ray decay curve only one of these assignments is accepted as being correct. If no resolution of the proper identification was attainable, then that gamma-ray transition was discarded.

(b) All the gamma-ray transitions for each isotope give consistent values for the production cross section of that isotope; or alternatively stated, that all the gamma-rays from a single radioactivity were observed with their proper relative abundances.

(c) All gamma-ray lines for a given radioactivity with intensities stronger than the weakest observed gamma-ray must have been present, unless they could have been shown to have been masked by an activity with a larger cross section.

(d) The energy of the accepted gamma-ray lines should have been reasonably close to the literature values, typically $\pm$ 0.2 keV. Assignments with large deviations were discarded.

4. Misidentifications

Due to the stringent screening procedure used the number of misidentified nuclides that have more than one observable gamma-ray transition is very small, probablly less than one per experiment. However, misidentifications can be made for those nuclides with only one transition. As it turns out such nuclei make up a large class that

spans the entire range of half-lives and transition energies observable in this study. Contributions from such misidentifications have been estimated to be ~1 in 50. These activities are usually recognized in the subsequent stages of data reduction by their improper behavior in the charge dispersion fitting.

E. Mass Yield Calculations

Having generated a self-consistent set of isotopic cross sections, the next step of the analysis is to fit the measured cumulative, partial cumulative and independent yields to a consistent set of charge dispersion curves. By the treatment of the measured yields in this way one is able to calculate $d\sigma^2/dZdA$ for the post neutron-charged particle emission reaction products, and from this quantity partial integration generates either $d\sigma/dA$ or $d\sigma/dZ$, colloquially referred to as the mass yield and charge yield, respectively.

1. Charge Dispersions

Because one needs to correct the radiochemically measured production cross sections for beta decay occurring between the time of the production of the nuclides in the nuclear reaction and the time that they are detected through their own beta decay the concept of charge dispersion fitting is conceptually attractive. A charge dispersion is simply a representation of the distribution of the total isobaric cross section, $\frac{d\sigma}{dA}$ or $\sigma(A)$, (mass yield) along that isobar. If one assumes that the distribution follows a Gaussian probability function then the independent yield cross section, $\sigma_{IY}(Z,A)$, can be written in terms of the mass yield as:[64]

$$\frac{d^2\sigma}{dZdA} = \sigma_{IY}(Z,A) = \sigma(A) \left\{ (\pi c)^{-\frac{1}{2}} \exp - \frac{(Z-Z_p(A))^2}{c} \right\} \qquad (4)$$

where $c = 2\sigma_Z(A)^2$ determines the width of the Gaussian and $Z_p(A)$ determines the centroid or most probable Z as a function of mass number, A. This formulation of the charge dispersion curve has three independent variables, $\sigma(A)$, $Z_p(A)$ and $\sigma_Z(A)$, so in order to uniquely specify this function one would need to measure three independent yield cross sections for each isobar. There are no isobars that contain three members that are shielded from beta decay.[65] However, one can calculate independent yield cross sections for cumulative yield isobaric members once the center and width of the Gaussian are known. Therefore, even if an isobar contains no independent yields, by starting with an assumed center and width for the Gaussian function one can find an iterative solution.

Again, the nature of the proposed study and of such radiochemical studies in general does not lend itself to the measurement of isobars. In such studies one finds a wide assortment of radionuclides are observable which span the periodic table with relatively few isobaric pairs.[18] A further assumption needs to be introduced in order to apply the Gaussian charge distributions to the measured data. That is, the value of $\sigma(A)$ is not changing rapidly as a function of A. If this is the case then one can construct a single charge dispersion curve for a limited range of isobars. So in practice one can bin the measured data by A and construct a charge dispersion curve for bin via an iterative procedure. However, extreme caution must be used in regions where the mass yield is changing rapidly, typically

near the masses of the projectile and target in heavy ion reactions.

The computer code used to calculate the independent and mass yields from the measured data was written by Otto.[66,11] The values of $Z_p(A)$ and $\sigma_Z(A)$ were input parameters that were iterated to obtain a set of calculated independent yields consistent with the Gaussian curves they were based on. An example of a final charge dispersion fit is shown in figure one for fission products from the $^{48}Ca + ^{159}Tb$ system. The measured data are the solid points and the calculated independent yields the open points. One can see that corrections for parent feedings are small. However, this approach did not work in the near target and projectile regions as expected.

2. Mass Dispersions

An alternative method that has been used to correct the radiochemically measured partial cumulative yields is fitting the data along constant Z values (isotopes) to mass dispersion curves.[18] This method is essentially the same as the charge dispersion analysis with the exception of a change of variables. One assumes that the mass dispersions are Gaussian and therefore can be described by the equation:

$$\frac{d^2\sigma}{dZdA} = \sigma(Z,A) = \sigma(Z) \left\{ (2\pi\ \sigma_A^2)^{-\frac{1}{2}} \exp\left[\frac{-(A-A_p(Z))^2}{2\sigma_A^2} \right] \right\} \qquad (5)$$

where the three variables $\sigma(Z) = \frac{d\sigma}{dZ}$, σ_A, and $A_p(Z)$ are the charge yield, the Gaussian width at constant Z and the most probable A value for constant Z, respectively. This analysis is reasonable because the function $\sigma(Z,A)$ is bivariant in Z and A with a measured correlation coefficient of $r^2 = 0.95$ for heavy ion induced reactions.[67]

The analysis of the data in this framework, though perhaps conceptually more difficult, has several advantages over charge dispersion analysis: (1) Because of the general stability of even-even nuclei the radiochemical method has an enhanced sensitivity to odd Z products, i.e. the number of even Z products that are observable is quite small. Thus an isobaric analysis will suffer from the deficiency of even Z products. However, the odd Z isotopic distributions will be correspondingly enhanced in the number of observable products due to the particular instability of odd-odd nuclei. (2) Because of the large number of odd Z yields generally one can construct good mass dispersion curves for the odd Z products with the mass dispersion curves for the even Z products typically missing or having only one measured yield. Thus one can avoid the problem of fitting "average" charge dispersion and the problem reduces to inferring the centers and width of the missing (or poorly described) even Z mass dispersions from the neighboring odd Z curves. This has the tremendous advantage that it can treat those areas where $d\sigma/dZ$, or alternatively $d\sigma/dA$, is rapidly varying. This can be seen in Figure 2 where the calculated independent yields from the ^{56}Fe + Ce reaction have been plotted versus A for the near-projectile products. Here the isobaric yield changes by a factor of 10 for 6 units of Z which would obviate "charge dispersion" fitting.

In practice both charge and mass dispersion fitting were applied to the data. First, the gross features of the product distributions were obtained from a charge dispersion analysis and used to construct the first fit in the mass dispersion analysis.

F. Thick Target Reaction Cross Sections

Because the projectiles are stopped in the target, the total reaction cross section that is observed in these experiments represents a weighted average over all energies from the incident (therefore highest) down to the interaction threshold. Thus one can write the weighted average reaction cross section, $\bar{\sigma}_R$, as:[18]

$$\bar{\sigma}_R = \frac{1}{E-B} \int_B^E \sigma_R(E)\, dE \qquad (6)$$

All energies are in the center of mass system and B is the interaction barrier. The variation of the reaction cross section with energy is well known[20-22] and has the form:

$$\sigma_R(E) = \pi R_{12}^2 \left(1 - \frac{V(R_{12})}{E}\right) \qquad (7)$$

where R_{12} is the center to center radial separation and $V(R_{12})$ the value of the ion-ion potential at that separation. This expression results from a simplification of the summation of the reaction cross section over the incoming partial waves[68-70,33,34] for incident energies large compared to $V(R_{12})$.

The one dimensional ion-ion potential, $V(R_{12})$, is usually written with three components, a coulomb term, a nuclear term and a centrifugal term.[71,68] The analysis is simplified by first considering only the s wave interaction threshold and by realizing that $V_{coul}(R_{12}) >> V_{nuc}(R_{12})$[11]; therefore reducing the potential to only a coulomb term,

$$V(R_{12}) \sim \frac{Z_1 Z_2 e^2}{R_{12}} = V_{coul}(R_{12}) \sim B \qquad (8)$$

This expression is, of course, independent of the incident energy, which allows one to evaluate the integral expression of equation (6) analytically.

$$\bar{\sigma}_R = \frac{\pi R_{12}^2}{E-B} \int_B^E \left(1 - \frac{B}{E}\right) dE \qquad (9)$$

$$\bar{\sigma}_R = \pi R_{12}^2 \left\{1 - \left(\frac{B}{E-B}\right) \ln \left(\frac{E}{B}\right)\right\} \qquad (10)$$

which gives the weighted average reaction cross section in terms of the single unknown parameter R_{12}.

There have been several parameterizations of reaction cross sections which have led to various prescriptions for the value of R_{12} in terms of the mass numbers (and therefore, the radii) of the reaction partners.[20,10] The values of R_{12}, $V_{coul}(R_{12})$ and $\bar{\sigma}_R$ are tabulated in Table V for the four systems studied in this work. Four prescriptions for the interaction radius were used: (1) $R_{12} = R_1 + R_2 + 1.7$ fm where $R_1 = 1.12\ A_1^{1/3} + 2.009\ A_1^{-1/3} - 1.513\ A^{-1}$ obtained by fitting ^{32}S induced fusion reaction (total reaction) excitation functions.[20] (2) $R_{12} = 1.16\ [A_1^{1/3} + A_2^{1/3} + 2]$ fm which corresponds to the separation distance at which the 10% density points of the two nuclei overlap.[72,40] (3) $R_{12} = C_1 + C_2 + \xi$ fm[10] where C_i is the half-density matter radius[72] used in the Proximity Force model[73] and $\xi \sim 4.5 - \left(\frac{C_1+C_2}{6}\right)$ fm from fitting elastic scattering reaction cross sections.[1] And (4) $R_{12} = 1.07(A_1^{1/3} + A_2^{1/3}) + 2.7$ fm suggested by Bass after fitting theoretical expressions to experimental interaction barriers for a wide range of projectile-target combinations.[74,75]

Table V shows that the first three prescriptions give values that are in reasonable agreement, with the values of $\bar{\sigma}_R$ being the most sensitive to the different calculations. The values calculated with Bass' prescription are significantly different.

Table V. Weighted Average Reaction Cross Sections

		R_{INT} (fm)	$V^{lab}_{coul}(R_{INT})$ (MeV)	$\bar{\sigma}_R$ (mb)	$\bar{E}^{lab}_{proj}$ (MeV)
$^{48}Ca+^{140}Ce$	1	12.48	179.7	1735.0	278.4
	2	12.56	178.6	1768.4	277.7
	3	12.62	177.7	1794.6	277.0
	4	12.14	173.5 *	1700.8	274.2
$^{48}Ca+^{159}Tb$	1	12.74	191.6	1681.3	286.3
	2	12.82	190.1	1723.0	285.3
	3	12.86	189.5	1740.0	284.9
	4	12.39	185.5 *	1653.5	282.3
$^{56}Fe+^{140}Ce$	1	12.67	239.6	1534.4	344.4
	2	12.78	237.9	1587.7	343.3
	3	12.83	237.0	1595.2	342.7
	4	12.35	233.4 *	1506.3	340.4
$^{56}Fe+^{159}Tb$	1	12.91	254.9	1466.0	354.0
	2	13.04	252.3	1517.4	352.4
	3	13.07	251.8	1528.6	352.1
	4	12.59	248.5 *	1444.2	350.0

Table V. (cont'd).

Footnotes

1 $R_{INT} = R_1 + R_2 + 1.7$ fm; $R_i = 1.12\ A_i^{1/3} + 2.009\ A_i^{-1/3} - 1.513/A_i$ fm

2 $R_{INT} = 1.16\ [A_1^{1/3} + A_2^{1/3} + 2]$ fm

3 $R_{INT} = C_1 + C_2 + \xi(R_{SA})$ fm; $\xi(R_{SA}) \sim 4.5 - \left(\frac{C_1+C_2}{6}\right)$ fm

4 $R_{INT} = 1.07(A_1^{1/3} + A_2^{1/3}) + 2.7$ fm

* $V_{INT}(R_{INT}) = \frac{Z_1 Z_2 e^2}{R_{INT}} - 2.9\left(\frac{A_1^{1/3}A_2^{1/3}}{A_1^{1/3}+A_2^{1/3}}\right)$ MeV , after R. Bass, Reference 74

Also contained in Table V are values for the calculated effective energy for the thick target experiments.[18] The effective energy is calculated by rearranging equation (7) to give:

$$\bar{E} = \frac{B}{1 - (\bar{\sigma}_R/\pi R_{12}^2)} \qquad (11)$$

Again, the first three prescriptions give reasonable agreement but Bass' value of R_{12} gives a somewhat lower value.

The cross sections for the ^{48}Ca induced reactions were normalized to the calculated values of $\bar{\sigma}_R$ to allow calculation of the component cross sections even though the absolute beam intensity was unknown. This is reasonable because previous radiochemical studies, where the absolute cross sections were known, have been shown to be in agreement with this weighted average cross section.[9,11,18,40,48]

III. RESULTS

A. Mass Distributions

The results of this study are contained in Tables VI through XI and in Figures 3 through 6. The measured cross sections along with the fractional independent yield and dynamite factor[76] are given for the nuclides observed in the work. The mass yield curves ($\frac{d\sigma}{dA}$ vs. A) from the study, Figures 3-6, show several striking features; first, the gross features indicate the sharp decline of evaporation residue products as the mass of the compound system increases. And secondly, in general terms, the relative proportions of the components of the mass distributions appear to be correlated with the projectile (entrance channel) rather than compound system. In Tables VII through X the most probable A value is tabulated as a function of product Z as well as the missing mass, $\nu = (A_1 + A_2) - (A_{p\ell} + A_{ph})$, assuming no charged particle evaporation.[40]

TABLE VI-A CA-48 + CE

ISOTOPE	CROSS SECTION (MB)	FRACTION CUMULATIVE	DYNAMITE FACTOR
NA- 24	1.5290E+00 +/- 1.3022E-03	.573	1.361
MG- 28	5.8058E-01 +/- 1.3321E-01	.743	2.103
S - 38	1.3046E+00 +/- 4.5080E-01	1.000	2.244
K - 42	8.0444E+00 +/- 5.9848E-03	1.000	3.253
K - 43	1.0651E+01 +/- 3.8865E+00	.476	1.207
CA- 47	1.2960E+02 +/- 9.4156E+00	1.000	1.673
SC- 44M	7.7998E-01 +/- 2.7813E-01	1.000	19.480
SC- 46	1.5864E+01 +/- 2.7839E-02	1.000	4.827
SC- 48	9.5119E+01 +/- 2.2868E+00	1.000	2.509
MN- 52	1.4528E+00 +/- 7.7063E-02	.984	10.728
MN- 56	3.1996E+01 +/- 7.2986E-01	.859	1.628
FE- 59	8.6458E+00 +/- 3.2691E-02	1.000	2.139
CO- 60	1.1944E+01 +/- 4.1418E-01	1.000	1.683
NI- 65	2.8735E+00 +/- 2.3509E+00	1.000	4.774
CU- 67	6.8121E+00 +/- 1.0427E-02	1.000	3.223
ZN- 69M	4.1431E+00 +/- 1.4127E-03	.924	2.336
ZN- 71M	1.4795E+00 +/- 2.1919E-01	1.000	3.805
GA- 72	7.7557E+00 +/- 1.0959E+00	.400	1.007
GA- 73	4.0429E+00 +/- 5.9688E-01	1.000	2.513
GE- 77	5.2939E+00 +/- 2.2132E+00	1.000	5.865
AS- 74	4.6270E+00 +/- 4.5962E-01	1.000	3.585
AS- 76	4.3984E+00 +/- 8.5175E-01	1.000	2.376
AS- 78	5.6133E+00 +/- 7.0126E-03	.185	.606
BR- 76	1.8818E+00 +/- 7.3040E-01	.995	24.677
BR- 77	1.4701E+00 +/- 4.5080E-01	.915	9.790

TABLE VI-A CA-48 + CE

ISOTOPE	CROSS SECTION (MB)	FRACTION CUMULATIVE	DYNAMITE FACTOR
BR- 82	5.0399E+00 +/- 3.5377E-01	1.000	3.677
KR- 88	7.7383E-01 +/- 4.0884E-01	1.000	46.719
RB- 82M	3.1996E+00 +/- 3.8825E-01	1.000	4.731
RB- 83	7.2518E+00 +/- 9.1671E-01	.817	2.560
RB- 84	7.3414E+00 +/- 2.0889E-02	1.000	2.495
Y - 86	1.8390E+00 +/- 2.7866E-01	.740	6.052
Y - 87M	7.9602E+00 +/- 4.3717E-01	.834	3.804
Y - 88	6.4299E+00 +/- 2.8655E-01	.990	3.031
ZR- 89	3.3626E+00 +/- 1.6399E-01	.874	5.105
SR- 92	6.3163E-01 +/- 1.8444E-03	1.000	18.539
Y - 90M	8.3424E+00 +/- 4.3516E-01	1.000	2.397
Y - 92	5.0814E+00 +/- 6.4379E-01	.530	2.073
ZR- 95	4.2006E+00 +/- 3.4655E-02	.860	4.348
ZR- 97	3.8679E-01 +/- 9.8540E-02	1.000	19.847
NB- 90	9.0334E-01 +/- 1.9941E-01	.896	14.843
NB- 95	8.3585E+00 +/- 1.0624E+00	.991	2.386
NB- 96	5.4997E+00 +/- 2.0769E-01	1.000	2.845
MO- 93M	1.0485E+00 +/- 2.3335E-02	1.000	10.785
TC- 95	1.2328E+00 +/- 1.4461E-01	.926	14.417
RU-103	1.2695E+01 +/- 1.9473E+00	.737	2.024
RU-105	2.4391E+00 +/- 7.8960E-02	.878	5.546
RH- 99M	1.8724E-01 +/- 1.0017E-03	.943	27.053
RH-100	1.1148E+00 +/- 5.5318E-02	.999	12.008
RH-101M	3.1528E+00 +/- 6.9070E-01	1.000	6.078
RH-105	7.0848E+00 +/- 7.3173E-01	.679	1.710
RH-106M	3.6246E+00 +/- 1.9379E-01	1.000	3.195

TABLE VI-A CA-48 + CE

ISOTOPE	CROSS SECTION (MB)	FRACTION CUMULATIVE	DYNAMITE FACTOR
PD-112	3.5083E+01 +/- 2.4445E+00	1.000	31.254
AG-106M	1.6533E+00 +/- 6.0998E-01	1.000	5.822
CD-111M	3.2517E+00 +/- 3.4295E-01	1.000	2.449
IN-110M	9.2820E-01 +/- 5.3540E-01	1.000	10.745
IN-111	2.2333E+00 +/- 1.9299E-01	.870	4.859
IN-116M	2.2226E+01 +/- 1.1277E+01	1.000	3.361
SB-113	1.4060E+02 +/- 8.3117E+01	1.000	61.988
SB-118M	3.3894E+00 +/- 9.0882E-03	1.000	2.590
SB-120B	2.3068E+00 +/- 1.7308E-01	1.000	2.393
SB-122	1.2363E+00 +/- 6.4152E-03	1.000	8.758
TE-119M	2.6396E+00 +/- 2.4926E-01	1.000	3.777
TE-121	2.3135E+00 +/- 1.7067E-01	.724	1.386
TE-123M	1.2184E+03 +/- 2.6971E+02	1.000	3.025
I -121	2.4979E+00 +/- 1.4554E-01	.917	4.777
I -123	6.0263E+00 +/- 3.1341E+00	.758	1.536
XE-123	8.2957E-01 +/- 6.0837E-04	.956	7.306
XE-127	7.0621E+00 +/- 1.8604E-01	.554	1.178
CS-129	6.5194E+00 +/- 3.6941E-01	.612	1.194
BA-128	7.7611E-01 +/- 3.1167E-01	.955	6.839
I -132	7.2559E-01 +/- 2.8908E-01	1.000	75.686
BA-133M	4.14[illegible]E+00 +/- 1.7441E-02	1.000	2.398
BA-139	4.4626E-01 +/- 3.9320E-01	.956	47.242
LA-131	1.2012E+00 +/- 5.9047E-01	.926	17.204
LA-132	3.7917E+00 +/- 2.3429E-01	.412	3.504
LA-140	3.6727E+00 +/- 4.3196E-01	1.000	12.741
CE-139	7.1262E+01 +/- 1.0631E+01	.494	1.245
CE-141	5.0520E+01 +/- 2.5233E-02	.860	4.216

TABLE VI-A CA-48 + CE

ISOTOPE	CROSS SECTION (MB)	FRACTION CUMULATIVE	DYNAMITE FACTOR
PR-138M	4.8341E+00 +/- 6.4072E-03	1.000	4.528
PR-142	1.0179E+01 +/- 6.8055E-02	1.000	2.802
PR-145	1.4341E+00 +/- 1.0389E+00	.925	12.504
EU-146	1.2024E+00 +/- 8.7621E-01	.939	14.439
GD-147	6.3056E+00 +/- 5.1121E-03	.963	61.208
EU-152M	1.0124E+00 +/- 1.6599E-01	1.000	12.659
TB-151	2.0168E+00 +/- 7.2077E-01	.851	2.817
TB-152	4.3677E+01 +/- 3.5604E-01	.741	1.761
TB-153	7.2599E+01 +/- 3.1555E+01	.456	.973
TB-154	3.5070E-01 +/- 9.3555E-04	1.000	2.410
DY-155	2.7732E-01 +/- 1.7441E-03	.686	1.496
TM-165	1.4728E+02 +/- 8.6592E-01	.288	1.053
LU-167	6.7360E+00 +/- 8.7193E+00	1.000	1.674
LU-169	1.1073E+00 +/- 2.8227E-01	.901	2.299
LU-171	3.4228E+00 +/- 5.7256E-01	.898	2.033
HF-170	3.4388E+00 +/- 2.7679E-01	1.000	3.838
HF-171	9.0240E-01 +/- 1.0909E-01	1.000	1.946
HF-173	4.2140E+00 +/- 7.6408E-01	.810	1.536
HF-175	4.9838E+00 +/- 7.1436E-01	.173	1.255
TA-177	5.8164E+00 +/- 4.0148E+00	.234	1.984
TA-178M	8.9439E-01 +/- 5.9220E-04	1.000	13.474
RE-181	8.7100E+00 +/- 1.1203E+00	.401	.977
RE-182	4.4171E+00 +/- 1.0411E+00	.802	3.972
OS-183M	5.8940E+00 +/- 2.7839E-01	.520	1.036
IR-184	9.7979E+00 +/- 8.7835E-01	.803	1.419
IR-185	7.0353E+00 +/- 2.6530E+00	.632	1.111

TABLE VI-B CA-48 + TB

ISOTOPE	CROSS SECTION (MB)	FRACTION CUMULATIVE	DYNAMITE FACTOR
NA- 24	1.1267E+00 +/- 1.1654E-03	.733	1.996
MG- 28	6.3942E-01 +/- 1.0147E-01	.850	4.074
S - 38	1.5415E+00 +/- 5.0605E-04	1.000	4.465
CL- 39	3.0208E+00 +/- 6.8609E-02	1.000	2.171
K - 42	8.7719E+00 +/- 4.3581E-03	1.000	2.422
K - 43	1.4105E+01 +/- 4.3794E+00	.657	1.598
CA- 47	1.1654E+02 +/- 6.3298E+00	1.000	2.825
SC- 44M	1.1376E+00 +/- 1.4127E-01	1.000	6.872
SC- 46	9.9059E+00 +/- 4.7825E-01	1.000	2.841
SC- 48	4.4357E+01 +/- 1.3227E+00	1.000	2.452
MN- 52	4.8256E-01 +/- 3.2878E-02	.999	23.660
MN- 56	1.5386E+01 +/- 1.0242E+00	.778	1.318
FE- 59	1.0147E+01 +/- 2.2841E+00	1.000	1.600
NI- 65	3.7597E+00 +/- 2.3455E-01	1.000	2.928
ZN- 69M	5.6011E+00 +/- 1.3183E-03	.874	1.704
ZN- 71M	1.4281E+00 +/- 2.5964E-01	1.000	7.959
ZN- 72	9.8108E-01 +/- 7.7989E-01	1.000	18.126
GA- 72	6.1308E+00 +/- 2.5569E-01	.585	2.263
GA- 73	4.3501E+00 +/- 6.8412E-01	1.000	5.732
AS- 74	4.2023E+00 +/- 2.3294E+00	1.000	2.457
AS- 76	7.6964E+00 +/- 4.1226E-01	1.000	2.827
BR- 77	2.0982E+00 +/- 2.5145E-02	.840	3.612
BR- 82	6.8683E+00 +/- 1.8948E-01	1.000	4.128
SR- 92	8.5231E-01 +/- 9.5840E-02	1.000	23.915
Y - 86	2.3455E+00 +/- 2.9579E-01	.716	4.903

TABLE VI-B CA-48 + TB

ISOTOPE	CROSS SECTION (MB)	FRACTION CUMULATIVE	DYNAMITE FACTOR
Y - 87	5.7540E+00 +/- 2.1363E-01	.831	3.342
Y - 87M	5.4863E+00 +/- 2.5248E-01	.816	3.279
Y - 88	9.2621E+00 +/- 2.4274E-02	.989	2.805
Y - 90M	9.5108E+00 +/- 4.0282E-01	1.000	2.453
Y - 92	7.4404E+00 +/- 1.2708E+00	.577	2.712
ZR- 89	4.1848E+00 +/- 5.3378E-01	.852	4.023
ZR- 95	6.5354E+00 +/- 2.4340E-02	.881	5.566
ZR- 97	1.1076E+00 +/- 5.5316E-04	1.000	29.016
NB- 90	1.5561E+00 +/- 3.7458E-01	.877	10.550
NB- 95	1.2459E+01 +/- 5.2573E-01	.992	2.497
NB- 96	8.6695E+00 +/- 2.3133E-01	1.000	3.195
MO- 93M	1.2723E+00 +/- 2.5679E-02	1.000	8.146
MO- 99	1.0433E+01 +/- 8.8011E-01	.826	3.237
TC- 95	1.6937E+00 +/- 7.4331E-02	.913	10.369
RU- 97	1.8283E+00 +/- 8.1208E-01	.933	15.390
RU-103	2.2109E+01 +/- 1.3476E-01	.782	1.948
RU-105	4.6925E+00 +/- 1.0469E+00	.919	6.112
RH-100	1.5656E+00 +/- 1.0425E-01	.888	15.500
RH-105	1.5093E+01 +/- 1.4647E+00	.716	1.617
RH-106M	5.2470E+00 +/- 4.5747E-01	1.000	2.964
PD-112	4.9756E+01 +/- 4.5403E+00	1.000	47.647
AG-106M	2.7369E+00 +/- 1.3476E-01	1.000	6.941
AG-110M	6.9612E+00 +/- 1.0901E+00	1.000	2.287
AG-111	1.6563E+01 +/- 9.3718E-02	.833	2.543
CD-111M	3.7370E+00 +/- 6.0313E-01	1.000	2.254
IN-110M	1.5781E+00 +/- 7.9671E-03	1.000	15.125

TABLE VI-B CA-48 + TB

ISOTOPE	CROSS SECTION (MB)	FRACTION CUMULATIVE	DYNAMITE FACTOR
IN-111	4.0911E+00 +/- 3.9565E-01	.920	6.055
SB-116M	2.0902E+00 +/- 7.7623E-04	1.000	7.470
SB-118M	5.5967E+00 +/- 3.0852E-01	1.000	2.603
SB-120B	5.0202E+00 +/- 1.8736E-01	1.300	2.250
SB-122	2.8847E+00 +/- 1.1471E+00	1.000	4.810
I -124	6.7461E+00 +/- 6.0042E-01	1.000	2.152
I -126	2.7376E+01 +/- 1.6717E-02	1.000	3.022
XE-121	1.7266E+00 +/- 8.5670E-01	.981	87.033
XE-127	1.0484E+01 +/- 5.9486E-01	.621	1.339
CS-127	5.7409E+00 +/- 5.2170E-01	.863	3.148
BA-128	1.6768E+00 +/- 8.3549E-02	.941	9.023
BA-129	1.2064E+00 +/- 3.1656E-01	.889	4.177
LA-131	1.3586E+00 +/- 6.0357E-01	.902	9.951
LA-132	4.2250E+00 +/- 4.7196E-01	.340	1.934
LA-140	7.9744E-01 +/- 5.3019E-02	1.000	21.949
CE-135	5.3165E+00 +/- 6.9882E-01	.857	3.693
CE-139	1.3908E+01 +/- 3.3120E-02	.405	1.166
CE-141	5.5616E+00 +/- 1.9607E+00	.893	6.328
PR-138M	3.6573E+00 +/- 8.5231E-02	1.000	3.441
ND-139M	3.9909E+00 +/- 4.1189E-01	.890	6.409
PM-148	5.2748E-01 +/- 1.8041E-01	1.000	5.614
EU-148	6.9048E+00 +/- 1.5956E+00	1.000	3.264
GD-149	3.6258E+00 +/- 7.9305E-03	.885	5.813
TB-151	3.4005E+00 +/- 9.8400E-01	.918	8.916
TB-152	2.4428E+00 +/- 1.1450E-03	.936	4.843
TB-153	5.5675E+00 +/- 2.5591E+00	.643	2.136
TB-155	1.8648E+01 +/- 1.027?E+01	.597	1.418

TABLE VI-B CA-48 + TB

ISOTOPE	CROSS SECTION (MB)	FRACTION CUMULATIVE	DYNAMITE FACTOR
TB-156	1.5364E+01 +/- 2.2789E-01	1.000	2.644
DY-15T	1.1567E+01 +/- 1.0140E-03	.634	1.525
HO-161	1.1208E+01 +/- 7.1726E-03	1.000	2.373
ER-160	2.5416E+00 +/- 8.2451E-01	1.000	6.146
ER-161	5.6355E+00 +/- 6.9553E-01	.805	3.258
LU-169	2.1919E+00 +/- 6.2223E-01	.725	2.316
LU-171	2.3682E+01 +/- 4.8388E+00	.553	1.318
HF-173	3.6456E+00 +/- 7.2823E-01	.612	1.461
TA-175	1.7866E+00 +/- 1.1654E+00	.674	1.679
TA-176	1.7346E+00 +/- 1.1091E+00	.499	1.193
RE-181	1.1164E+00 +/- 6.1206E-01	.864	1.312
RE-182	2.7442E+00 +/- 3.8372E-01	.746	1.191
OS-183M	6.3430E-01 +/- 4.2740E-01	.920	1.600
AU-191	1.3220E+00 +/- 4.6244E-01	.805	1.196
AU-194	1.2554E-01 +/- 8.2890E-03	1.000	9.324
HG-192	5.0422E-01 +/- 1.9168E-01	.975	2.857
TL-196M	4.6303E-01 +/- 2.9498E-01	1.000	1.475
TL-198M	5.9955E-01 +/- 2.4889E-01	1.000	3.257
PB-201	4.2945E-01 +/- 2.3309E-03	.160	.904

TABLE VI-C FE-56 + DE

ISOTOPE	CROSS SECTION (MB)	FRACTION CUMULATIVE	DYNAMITE FACTOR
AR- 41	2.6079E+00 +/- 9.7167E-04	1.000	10.018
K - 43	2.0984E+00 +/- 1.2463E-01	.996	6.361
SC- 44	2.0146E-01 +/- 4.2800E-02	1.000	2.500
SC- 44M	3.6822E-01 +/- 8.7420E-02	1.000	2.500
SC- 46	2.0674E+00 +/- 7.3774E-02	1.000	1.577
CA- 47	2.5017E-01 +/- 1.5493E-02	1.000	218.489
SC- 47	2.2115E+00 +/- 2.4996E-02	.971	3.124
SC- 48	9.5824E-01 +/- 7.4965E-02	1.000	12.508
V - 48	8.9283E-01 +/- 2.1461E-02	.989	4.098
MN- 52	1.3414E+00 +/- 6.9009E-02	.993	7.702
MN- 56	7.7976E+00 +/- 5.8764E-01	.966	1.786
CO- 56	1.6802E+01 +/- 4.0851E-02	.995	16.140
CO- 57	2.5754E+01 +/- 1.5699E-01	.979	4.126
NI- 57	3.1645E-01 +/- 3.5566E-03	1.000	201.327
CO- 58	3.1992E+01 +/- 4.2172E-02	1.000	1.973
FE- 59	2.8851E+00 +/- 2.5039E-01	1.000	5.599
CU- 60	4.4208E+00 +/- 6.9204E-02	.996	37.366
CU- 61	1.7711E+01 +/- 1.2630E+00	1.000	7.714
ZN- 62	2.6829E+00 +/- 1.8019E-01	1.000	58.880
ZN- 63	1.5760E+01 +/- 1.7956E-01	.989	10.998
ZN- 65	2.0040E+01 +/- 2.2310E-01	.892	1.748
GA- 67	1.2472E+01 +/- 1.3111E+00	.914	2.085
ZN- 69M	7.5897E-01 +/- 2.5949E-03	.985	11.722
GE- 69	4.5638E+00 +/- 1.7651E-02	.931	2.564
AS- 71	3.3226E+00 +/- 5.1334E-03	.945	3.252

TABLE VI-C FE-56 + CE

ISOTOPE	CROSS SECTION (MB)	FRACTION CUMULATIVE	DYNAMITE FACTOR
SE- 73	1.5069E+00 +/- 2.0326E-03	1.000	4.249
AS- 74	2.1248E+00 +/- 8.3521E-02	1.000	2.203
SE- 75	5.2785E+00 +/- 8.7095E-01	.766	1.373
BR- 75	1.4605E+00 +/- 3.9010E-04	.962	5.707
BR- 77	2.1190E+00 +/- 6.9594E-02	.805	1.541
RB- 81	1.8671E+00 +/- 9.2618E-02	.859	2.109
BR- 82	7.5074E-01 +/- 4.6699E-02	1.000	43.807
RB- 82M	2.1324E+00 +/- 1.3869E-01	1.000	1.903
RB- 83	4.3883E+00 +/- 8.3824E-02	.584	1.186
RB- 84	2.5580E+00 +/- 3.0519E-02	1.000	2.941
Y - 85M	4.4620E-01 +/- 4.2549E-04	1.000	3.646
Y - 86	2.8353E+00 +/- 2.4432E-01	.701	1.601
ZR- 88	3.4006E+00 +/- 1.8164E-01	.859	2.280
Y - 88	3.6129E+00 +/- 5.4930E-02	.364	.807
ZR- 89	3.9443E+00 +/- 1.4623E-01	.745	1.515
Y - 90M	2.0306E+00 +/- 8.1268E-02	1.000	6.545
NB- 90	1.7350E+00 +/- 1.2502E-01	.827	2.646
Y - 91M	1.2964E+00 +/- 4.5529E-01	1.000	16.678
SR- 91	8.6597E-01 +/- 7.0048E-01	.994	515.080
Y - 92	5.3132E+00 +/- 1.2099E+00	.965	52.707
MO- 93M	1.4768E+00 +/- 2.5710E-02	1.000	2.505
TC- 93	3.9335E-01 +/- 6.8489E-02	.958	11.546
NB- 95	9.8141E-01 +/- 7.2951E-02	.888	6.427
TC- 95	2.1216E+00 +/- 1.7122E-01	.844	2.487
RU- 97	1.6657E+00 +/- 1.4213E-01	.877	3.155

TABLE VI-C FE-56 + CE

ISOTOPE	CROSS SECTION (MB)	FRACTION CUMULATIVE	DYNAMITE FACTOR
MO- 99	2.0824E-01 +/- 1.8855E-02	.971	30.337
RH-100	1.7558E+00 +/- 8.3889E-02	.795	2.235
RH-101M	2.4627E+00 +/- 1.2970E-02	1.000	2.218
AG-104	1.2279E+00 +/- 4.4641E-04	.749	3.134
RH-105	1.0366E+00 +/- 1.9000E-01	.914	T.345
AG-105	2.5797E+00 +/- 2.2526E-01	.793	2.181
AG-106M	1.8599E+00 +/- 5.2222E-02	1.000	2.262
IN-108M	5.6013E-01 +/- 2.5126E-02	1.000	7.162
IN-110M	1.4625E+00 +/- 1.3865E-03	1.000	2.738
IN-111	3.3118E+00 +/- 1.4326E-01	.666	1.544
CD-111M	1.0159E+00 +/- 3.7623E-01	1.000	3.530
SB-115	4.0504E+00 +/- 9.0972E-04	.709	1.961
SB-116M	3.1104E-01 +/- 1.0787E-01	1.000	2.386
TE-117	2.0035E+00 +/- 1.7727E+00	.779	2.494
SB-118M	9.3290E-01 +/- 4.2150E-02	1.000	3.052
TE-119M	1.6862E+00 +/- 1.5476E-01	1.000	2.412
I -120	4.3970E-01 +/- 1 1198E+00	.600	1.690
I -120M	1.1696E+00 +/- 5.6316E-04	1.000	2.819
I -121	5.5861E+00 +/- 5.0879E-01	.558	1.372
TE-121	6.1948E+00 +/- 1.1480E-02	.336	1.215
XE-123	4.7219E+00 +/- 3.9854E-01	.666	1.741
I -123	7.3644E+00 +/- 2.2310E-01	.388	1.199
XE-125	9.0755E+00 +/- 8.4474E-01	.454	1.257
CS-125	7.0828E+00 +/- 3.1624E-03	.685	1.986
XE-127	6.9529E+00 +/- 9.2055E-02	.278	1.505

TABLE VI-C FE-56 + CE

ISOTOPE	CROSS SECTION (MB)	FRACTION CUMULATIVE	DYNAMITE FACTOR
CS-127	4.1804E+00 +/- 8.1225E-01	.496	1.290
BA-128	5.4800E+00 +/- 9.3571E-01	.664	1.795
BA-131	1.0200E+01 +/- 1.4393E-01	.362	1.281
LA-131	4.9536E+00 +/- 1.1928E+01	.566	1.485
LA-132	5.8699E+00 +/- 2.1877E-03	.309	.819
CE-133	1.7837E+00 +/- 4.0244E-01	1.000	1.850
CE-135	7.1240E+00 +/- 1.3340E+00	.454	1.282
ND-136	2.7855E+00 +/- 5.0966E-01	1.000	4.208
CE-137M	3.6800E+00 +/- 2.3414E-01	1.000	4.835
PR-138M	3.7710E+00 +/- 8.5687E-01	1.000	3.064
CE-139	4.6439E+01 +/- 9.3506E-02	.079	1.081
ND-139M	3.0974E+00 +/- 1.7763E-01	.553	1.495
CE-141	9.8878E+00 +/- 4.9017E-02	.938	57.004
CE-143	3.8793E-01 +/- 7.1781E-03	.964	402.281
EU-145	1.8149E+00 +/- 1.8745E-02	.699	2.446
EU-146	8.7355E-01 +/- 7.1933E-02	.614	1.817
GD-146	1.1190E+00 +/- 1.1967E+00	1.000	5.898
EU-147	2.6144E+00 +/- 9.5152E-02	.522	1.471
·D-147	1.1486E+00 +/- 7.0936E-02	.729	3.008
TB-152	2.6988E-01 +/- 2.6750E-02	.545	1.580
RE-182	2.9804E-01 +/- 7.7023E-02	.283	1.280
PT-191	2.0092E+00 +/- 5.2937E-02	.247	1.303

TABLE VI-D FE-56 + TB-159

ISOTOPE	CROSS SECTION (MB)	FRACTION CUMULATIVE	DYNAMITE FACTOR
NA- 24	1.6732E-01 +/- 7.2225E-04	.925	1.056
K - 42	6.7392E-01 +/- 6.8931E-03	1.000	1.466
SC- 46	1.9958E+00 +/- 1.6373E-02	1.000	1.331
CA- 47	4.1742E-01 +/- 7.7193E-03	1.000	126.414
SC- 48	1.1043E+00 +/- 2.8431E-02	1.000	7.628
V - 48	5.6457E-01 +/- 5.7753E-02	.998	8.477
CR- 51	3.0834E+00 +/- 3.9285E-01	.987	2.832
MN- 52	8.4996E-03 +/- 2.2143E-01	.999	18.115
CO- 56	1.8136E+00 +/- 7.3926E-02	.999	44.086
MN- 56	8.8776E+00 +/- 3.1050E-01	.972	2.217
CO- 57	3.2724E+01 +/- 5.7672E-01	.994	6.799
CO- 58	6.3180E+00 +/- 1.7002E-01	1.000	2.274
FE- 59	3.6369E+00 +/- 1.0300E-01	1.000	4.698
CO- 60	2.8647E+00 +/- 2.1527E-02	1.000	1.686
GA- 67	5.0301E+00 +/- 7.6005E-01	.960	2.394
ZN- 69M	6.1209E-01 +/- 8.2188E-04	.994	13.220
GE- 69	3.6720E+00 +/- 7.9731E-01	.970	3.069
AS- 71	2.2002E+00 +/- 2.0679E-03	.978	4.095
AS- 72	3.0429E+00 +/- 9.5391E-02	.940	1.876
SE- 73	9.7254E-01 +/- 4.1445E-04	1.000	5.687
AS- 74	1.9869E+00 +/- 2.0736E-02	1.000	1.962
BR- 75	8.0946E-01 +/- 1.6899E-01	.987	8.225
AS- 76	2.4062E+00 +/- 1.7647E-01	1.000	12.136
KR- 76	2.5971E-01 +/- 4.5306E-02	1.000	67.376
BR- 77	1.4753E+00 +/- 1.7574E-01	.873	1.555

TABLE VI-D FE-56 + TB-159

ISOTOPE	CROSS SECTION (MB)	FRACTION CUMULATIVE	DYNAMITE FACTOR
RB- 81	1.0106E+00 +/- 2.7891E-04	.922	2.261
BR- 82	3.2400E-01 +/- 7.2981E-02	1.000	85.055
RB- 82M	1.2633E+00 +/- 2.9457E-02	1.000	1.709
RB- 83	3.3696E+00 +/- 9.1098E-02	.627	1.126
RB- 84	1.9478E+00 +/- 3.6180E-02	1.000	2.801
Y - 86	1.3662E+00 +/- 1.3756E-01	.801	1.736
Y - 87	3.3723E+00 +/- 1.4348E-02	.762	1.305
Y - 88	2.5836E+00 +/- 3.6936E-02	.394	.777
ZR- 89	2.4791E+00 +/- 6.7095E-03	.815	1.478
Y - 90M	1.0867E+00 +/- 4.3929E-02	1.000	7.804
NB- 90	1.0911E+00 +/- 5.8509E-02	.908	3.052
TC- 93	1.8851E-01 +/- 4.6197E-02	.986	19.766
MO- 93M	9.7497E-01 +/- 6.1209E-02	1.000	2.387
NB- 95	1.0471E+00 +/- 9.7524E-02	.951	8.528
TC- 95	1.5412E+00 +/- 8.3700E-02	.912	2.702
TC- 96	1.6394E+00 +/- 2.8323E-01	1.000	1.969
NB- 96	5.7672E-01 +/- 7.5654E-02	1.000	29.878
RU- 97	1.0090E+00 +/- 4.4118E-02	.937	3.632
MO- 99	2.6311E-01 +/- 3.3696E-02	.992	62.315
RH-100	1.0733E+00 +/- 1.6694E-01	.875	2.402
RH-101M	1.7102E+00 +/- 9.7470E-03	1.000	1.959
AG-104	7.2954E-01 +/- 1.7350E-04	.866	4.122
AG-106M	1.4008E+00 +/- 4.6116E-02	1.000	1.978
IN-108M	3.7476E-01 +/- 1.0519E-01	1.000	10.207
AG-110M	4.6764E-01 +/- 1.8535E-01	1.000	10.031

TABLE VI-D FE-56 + TB-159

ISOTOPE	CROSS SECTION (MB)	FRACTION CUMULATIVE	DYNAMITE FACTOR
IN-110M	1.1594E+00 +/- 2.5607E-01	1.000	2.605
CD-111M	6.5718E-01 +/- 1.0527E-01	1.000	3.332
IN-111	2.4062E+00 +/- 1.0870E-01	.748	1.509
IN-114M	7.7031E-01 +/- 1.2050E-01	1.000	4.459
TE-116	1.3254E+00 +/- 2.8431E-01	1.000	5.673
SB-116M	1.1910E+00 +/- 7.6437E-02	1.000	2.068
TE-117	1.4323E+00 +/- 3.3642E-04	.875	2.869
SB-118M	9.2988E-01 +/- 9.3123E-02	1.000	2.672
TE-119M	1.4253E+00 +/- 3.5937E-02	1.000	2.041
I -119	1.5522E+00 +/- 4.7952E-01	.871	3.783
TE-121	2.6954E+00 +/- 3.1320E-01	.352	1.147
I -124	4.1850E-01 +/- 4.9464E-02	1.000	4.087
XE-122	1.0978E+00 +/- 9.0990E-03	1.000	2.938
XE-123	1.2690E+00 +/- 1.0446E-01	.775	1.840
XE-125	3.0186E+00 +/- 2.8323E-01	.510	1.176
XE-127	3.5397E+00 +/- 2.2915E-01	.262	1.371
BA-128	1.8044E+00 +/- 1.7998E-01	.781	1.942
CS-129	3.7341E+00 +/- 1.9178E-01	.312	1.188
LA-131	2.3050E+00 +/- 2.1559E-01	.693	1.601
BA-131	8.2593E+00 +/- 2.1927E+00	.392	1.171
CE-132	1.4988E+00 +/- 6.3639E-02	.863	3.290
CE-135	2.1090E+00 +/- 2.3765E-01	.543	1.243
CE-139	3.3318E+00 +/- 4.8303E-02	.071	1.088
ND-139M	9.0018E-01 +/- 1.0738E-01	.685	1.601
EU-145	3.2454E+00 +/- 3.6531E-01	.840	3.363

TABLE VI-D FE-56 + TB-159

ISOTOPE	CROSS SECTION (MB)	FRACTION CUMULATIVE	DYNAMITE FACTOR
EU-147	3.6639E+00 +/- 1.0684E-01	.660	1.587
GD-147	2.7162E+00 +/- 1.8225E-01	.869	4.745
TB-148A	2.2054E-01 +/- 6.1857E-02	1.000	15.128
EU-148	8.4375E-01 +/- 2.9862E-02	.992	2.366
GD-149	4.1850E+00 +/- 3.2157E-01	.739	1.976
TB-151	1.2644E+01 +/- 3.3534E+00	.781	2.486
TB-152	2.6193E+00 +/- 4.0419E-01	.678	1.739
GD-153	5.0922E+00 +/- 3.1833E-01	.239	1.006
TB-153	1.8079E+00 +/- 1.3500E+00	.454	1.093
DY-155	5.1462E+00 +/- 1.8206E+00	.651	1.633
TB-155	9.4554E+00 +/- 2.0066E+00	.361	1.189
TB-156	3.8880E+00 +/- 7.7436E-02	1.000	4.746
HO-156	2.3466E+00 +/- 9.6822E-01	.786	2.873
DY-157	8.6778E+00 +/- 6.6420E-04	.421	1.169
HO-159	1.6146E+01 +/- 3.7179E+00	.252	.640
ER-159	3.3129E+00 +/- 1.0816E-01	1.000	2.600
TB-160	5.2407E+00 +/- 2.8053E-01	1.000	76.102
ER-160	4.5387E+00 +/- 9.4446E-01	1.000	1.861
HO-160	3.1320E+00 +/- 6.0831E-01	.669	1.983
ER-161	5.0679E+00 +/- 1.8492E-01	.543	1.356
TM-162	3.0051E+00 +/- 3.8367E-03	.483	1.529

Table VII. Most Probable A Value, ^{48}Ca + Ce

Z_1	A_{p1}*	Z_h	A_{ph}*	υ**
12	~28	66	152.9	7.1
13	"	65	150.6	
14	"	64	"	
15	"	63	148.8	
16	"	62	"	
17	"	61	"	
18	"	60	"	
19	42.8	59	141.0	4.2
20	45.5	58	137.8	4.7
21	47.7	57	134.6	5.7
22	"	56	132.1	
23	"	55	129.4	
24	"	54	127.1	
25	54.8	53	123.8	9.4
26	57.0	52	"	
27	"	51	118.7	
28	"	50	"	
29	"	49	114.0	
30	"	48	"	
31	71.1	47	109.1	7.7
32	73.7	46	"	
33	76.1	45	103.9	8.0
34	"	44	101.5	
35	79.6	43	98.2	10.2
36	"	42	"	
37	84.2	41	94.4	9.4
38	86.9	40	91.9	9.2
39	89.6	39	89.6	8.8

* errors in A_p on the order of $\leq \pm 0.5$ amu

** $\upsilon = (A_1 + A_2^p) - (A_{p1} + A_{ph})$

Table VIII. Most Probable A Value, ^{48}Ca + Tb

Z_1	A_{p1}*	Z_h	A_{ph}*	ν**
17	38.6	68	-	
18	-	67	159.9	
19	43.0	66	157.3	6.7
20	45.5	65	155.0	6.5
21	47.7	64	152.0	7.3
22	-	63	150.0	
23	-	62	-	
24	-	61	-	
25	55.2	60	-	
26	57.5	59	-	
27	-	58	138.0	
28	62.7	57	135.0	9.3
29	-	56	132.0	
30	68.7	55	129.0	9.3
31	71.4	54	125.5	10.1
32	-	53	123.0	
33	75.7	52	-	
34	-	51	118.2	
35	80.3	50	-	
36	0	49	113.5	
37	-	48	-	
38	87.1	47	109.0	10.9
39	89.7	46	-	
40	92.3	45	104.4	10.3
41	94.1	44	101.1	11.8
42	96.6	43	-	

* errors in A_p are on the order of $\leq \pm 0.5$ amu

** $\nu = (A_1 + A_2) - (A_{p1} + A_{ph})$

Table IX. Most Probable A Values, ^{56}Fe + Ce

Z_l	A_{pl}*	Z_h	A_{ph}*	ν**
18	39.9	66	-	
19	42.1	65	151.0	2.9
20	44.7	64	148.5	2.8
21	46.6	63	146.2	3.2
22	-	62	-	
23	50.5	61	-	
24	-	60	-	
25	54.4	59	-	
26	56.0	58	136.1	3.9
27	57.8	57	-	
28	60.0	56	130.6	5.4
29	61.9	55	-	
30	64.1	54	124.6	7.3
31	67.5	53	121.6	6.9
32	70.2	52	118.6	7.2
33	72.3	51	115.6	8.1
34	74.7	50	-	
35	76.2	49	111.3	8.5
36	-	48	-	
37	82.9	47	106.9	6.2
38	-	46	-	
39	87.3	45	102.2	6.5
40	89.7	44	99.5	6.8
41	92.2	43	96.8	7.0
42	94.5	42	94.5	7.0

* errors in A_p are on the order of $\leq \pm 0.5$ amu
** $\nu = (A_1 + A_2) - (A_{pl} + A_{ph})$

Table X. Most Probable A Values, ^{56}Fe + Tb

Z_l	A_{pl}*	Z_h	A_{ph}*	ν**
19	42.0	72	-	
20	44.3	71	-	
21	46.7	70	-	
22	-	69	162.5	
23	50.1	68	160.2	4.7
24	52.3	67	158.1	4.6
25	54.5	66	155.7	4.8
26	56.0	65	154.4	4.6
27	58.9	64	148.5	7.6
28	-	63	146.1	
29	-	62	-	
30	-	61	-	
31	68.2	60	-	
32	70.3	59	-	
33	72.6	58	133.4	9.0
34	74.7	57	131.4	8.9
35	76.7	56	129.4	8.9
36	78.8	55	127.4	8.8
37	83.0	54	125.2	6.8
38	-	53	120.7	
39	88.0	52	118.7	8.3
40	90.3	51	116.0	8.7
41	92.5	50	-	
42	-	43	111.5	
43	96.9	48	108.9	9.2
44	99.1	47	106.7	9.2
45	102.0	46	-	

* errors in A_p are on the order of $\leq \pm 0.5$ amu

** $\nu = (A_1 + A_2^p) - (A_{pl} + A_{ph})$

As in previous studies of heavy ion induced nuclear reactions the mass (charge) distributions of the products seem to suggest Gaussian shapes.[18,24,26] In the past the mass yield curve has been divided into contributions from macroscopic reaction channels on the sole basis of these different Gaussian components.[18,16] There are three reaction channels open to the systems in this work, the quasielastic transfer reaction (QET) characterized as peripheral or grazing collisions where only a few nucleons can be exchanged,[77,78] the deep inelastic transfer reaction (DIT) thought to represent more solid collisions where a dynamical equilibrium exists between the reaction partners,[10,79,80] and complete fusion (CF) or compound nucleus formation where the "completely fused" system de-excites by particle emission or fission on a time scale much longer than the collision time.[8]

While this division is possible in this study, the distinction between QET and DIT is a kinematical one and there is no kinematical information in a mass yield curve.[2] Using previous countertelescope studies as a guide,[24,26] the contributions to the mass distribution curves were obtained by the component analysis shown in Figures 3 through 6. One notes that evaporation residue (ER) products, curve A, are only visible in the lighter systems and that complete fusion-fission (CF-f), curve B, becomes less important for the ^{56}Fe induced reactions. The DIT products are represented by curves C and D and the QET transfer products are represented by curves E and F. The fractions of the reaction cross section that these reaction mechanisms make up are given in Table XI. While not specifically shown, the cross section for the DIT light fragments, C, is approximately equal to the cross section

for the DIT heavy fragments, D. The same is also true for the QET cross sections, E and F.

B. Complete Fusion

The results for the fraction of the total reaction cross section, σ_R, that goes into complete fusion, CF, are given in Table XI. The immediately striking feature of these results is that the fraction of σ_R that is represented by CF processes seems to be determined by the projectile, and not by the target, nor by the compound system. It is interesting to note that for the ^{48}Ca induced reactions the CF cross section is divided differently between ER and CF-f for the two targets (reflecting the different fission competition in the compound nuclei) but comes up to the same total fraction. And as mentioned previously, there were no evaporation residues detected for the ^{56}Fe induced reactions due to their relatively low production cross sections.

Table XI. Macroscopic Reaction Channel Cross Sections

	^{48}Ca + Ce		^{48}Ca + Tb		^{56}Fe + Ce		^{56}Fe + Tb	
	percent	(mb)	percent	(mb)	percent	(mb)	percent	(mb)
σ_{ER}	14 ± 2	(247)	≤ 1	(≤ 24)	<< 1		<< 1	
σ_{CF-f}	20 ± 3	(353)	33 ± 3	(561)	6 ± 1	(98)	5 ± 2	(78)
σ_{CF}	34 ± 4	(600)	34 ± 4	(585)	6 ± 1	(98)	5 ± 2	(78)
σ_{QET}	29 ± 3	(512)	29 ± 3	(496)	50 ± 6	(820)	60 ± 7	(940)
σ_{DIT}	37 ± 4	(653)	37 ± 4	(634)	44 ± 3	(720)	35 ± 3	(550)

IV. DISCUSSION

It has become standard to describe the limitation of complete fusion in heavy ion reactions in terms of a critical angular momentum.[81-83,70,74] This description is based on a partial wave analysis of the reaction where the reaction cross section is written in the form:[68]

$$\sigma_R = \pi\lambda\!\!\!^{-2} \sum_{\ell=0}^{\infty} (2\ell+1)\, T_\ell \qquad (12)$$

where $\lambda\!\!\!^{-}$ is the reduced wavelength of the heavy ion projectile and T_ℓ is a transmission coefficient through a one dimensional (radial) fusion barrier. The values of T_ℓ range from 1, pure transmission, to 0, no transmission. Because of the properties of the T_ℓ's and the large values of ℓ, it is conventional to introduce sharp cutoff ℓ values.[84] Thus $T_\ell = 1$ when $\ell \leq \ell_{max}$ and $T_\ell = 0$ when $\ell > \ell_{max}$, which gives:

$$\sigma_R = \pi\lambda\!\!\!^{-2} \sum_{\ell=0}^{\ell_{max}} (2\ell + 1) \qquad (13)$$

Therefore, when it was found that the complete fusion cross section was less than the reaction cross section a lower ℓ value cutoff to complete fusion appeared in a very natural way.[85] So one can write the complete fusion cross section in a form analogous to Equation 13 as:

$$\sigma_{CF} = \pi\lambda\!\!\!^{-2} \sum_{\ell=0}^{\ell_{crit}} (2\ell + 1) \qquad (14)$$

where ℓ_{crit} is the sharp cutoff critical angular momentum for fusion. Implicit in this expression is the assumption that large ℓ values (grazing collisions) do not lead to fusion. This picture has been

extended with the inclusion of deep inelastic collisions in the region that intervenes between low ℓ - complete fusion and high ℓ - elastic transfer.[81] This picture of the ℓ dependence of the reaction channels is shown schematically in Figure 7.[86] In the next sections the critical angular momenta are deduced and compared to model calculations.

A. Deduced Critical Angular Momenta

The maximum angular momentum that can be brought into the reaction has been analyzed in terms of Fresnel diffraction[87] and in turn related to the quarter point angle in elastic scattering experiments.[88] The quarter point angle is defined as the center of mass angle at which the ratio of measured elastic scattering cross section to the calculated Rutherford[89] cross section is 0.25. The measured cross section for elastic scattering drops below the Rutherford cross section with the onset of nuclear reactions. Thus the radial separation at which nuclear reactions begin to dominate and elastic scattering is no longer possible can be written:

$$R_{12} = \eta \star \left[1 + \operatorname{cosec}\left(\frac{\theta_Q}{2}\right)\right] \qquad (15)$$

where θ_Q is the quarter point angle and η is the Sommerfeld parameter equal to the distance of closest approach on a classical orbit divided by the reduced wave length:

$$\eta = \frac{Z_1 Z_2 e^2}{\hbar[2E/\mu]^{\frac{1}{2}}} \quad , \quad \mu = \frac{m_1 m_2}{(m_1+m_2)} \quad . \qquad (16)$$

The maximum angular momentum, ℓ_{max}, is related to the quarter point angle the expression:

$$\ell_{max} = \eta \cot(\frac{\theta_Q}{2}) \qquad (17)$$

No elastic scattering studies have been done for any of the systems studied in this work, however, from the systematics of R_{12} detailed above one can calculate θ_Q and then in turn ℓ_{max} once a value for R_{12} has been chosen. The average value of entries 1, 2 and 3 from Table V was used for R_{12} in these calculations, and the results are given in Table XII. One can see that the angular momenta brought into these systems is quite high on the order of 150 $\hbar$ units.

Using the sharp cutoff model and the angular momentum fractionation shown schematically in Figure 7 the ℓ cutoff values for the three reaction channels are given in Table XII. Again, because of the nature of the experiment, the actual ℓ cutoff values between QET and DIT may be somewhat different. A striking feature is the factor of the difference in ℓ_{crit} between the ^{48}Ca and ^{56}Fe induced reactions. This difference is also seen in Table XIII where four different reactions that produce an At (or nearly At) compound nucleus at nearly the same excitation energy are compared.[85,28] As in the earliest experiment where complete fusion was studied as a function of entrance channel,[90] the comparison shows that the role of complete fusion is determined in the dynamics of the entrance channel and not by the equilibrium properties of the compound nuclei. These cutoff values are plotted versus $Z_{projectile}$ in figure 8, along with the ℓ_{max} for the reaction. This figure indicates the ℓ_{crit} value is restricted by kinematics for low Z_{proj}, and therefore seems to go through a maximum in the Ar-Ca region.

Table XII. Calculated ℓ_{max} and ℓ_{crit} Values

	$^{48}Ca + ^{140}Ce$	$^{48}Ca + ^{159}Tb$	$^{56}Fe + ^{140}Ce$	$^{56}Fe + ^{159}Tb$
E_{CM} (MeV)	205.5	216.6	242.9	258.9
R_{12}* (fm)	12.55	12.80	12.76	13.01
λ* (fm)	.05325	.05107	.04630	.04408
η	76.20	84.48	96.39	106.5
ℓ_{max} ($\hbar$ units)	140	143	151	156
	$\ell_1 - \ell_2$	$\ell_1 - \ell_2$	$\ell_1 - \ell_2$	$\ell_1 - \ell_2$
QET	118 - 140	121 - 143	107 - 151	99 - 156
DIT	81 - 117	83 - 120	35 - 106	34 - 99
CF	0 - 80	0 - 82	0 - 35	0 - 34

* average value of entries 1, 2 and 3 in Table V

Table XIII. Comparison of Critical ℓ Values for the Compound System, At

System	CN	E_{lab} (MeV)	ℓ_{max} ($\hbar$)	E* (MeV)	σ_{CF} (mb)	ℓ_{cr}[1] ($\hbar$)	Reference
$^{12}_{6}C+^{197}_{79}Au$	$^{209}_{85}At$	126	70	102	1403 ± 421	53 ± 8	Natowitz, 85
$^{40}_{18}Ar+^{165}_{67}Ho$	$^{205}_{85}At$	225	99	93	860 ± 90	86 ± 5	Hanappe et al., 28
$^{48}_{20}Ca+^{159}_{65}Tb$	$^{207}_{85}At$	217[2]	143	116	585 ± 60	82 ± 8	this work
$^{56}_{26}Fe+^{140}_{58}Ce$	$^{196}_{84}Po$	243[2]	151	108	126 ± 16	34 ± 5	this work

1 The experimental critical ℓ value calculated as $\ell^2\hbar^2 = \sigma_{CF}/\pi\lambda^2$.

2 Effective bombarding energies for thick targets, discussed in text.

B. Comparisons with Reaction Model Calculations of ℓ_{crit}

Because of the "thick" target nature of the experiments of this work and the "thin" target nature of theoretical calculations one must be cautious about direct comparison of radiochemical work with theoretical calculations. However, the recent calculations of Birkelund et al.[91] do show that the situation may not be as bad as might be imagined. These calculations, and their comparison with data, indicate that the dependence of σ_{CF} on energy follows the simple form of equation (7) with the exception of the very high and very low energy regions.[91] This would indicate that the "effective energy" previously calculated should be approximately correct and any strong deviations of calculated quantities from the experimentally measured values are to be considered serious discrepancies.

The measured values of the critical angular momentum for fusion have been given in Table XIII. In the following sections various prescriptions for ℓ_{crit} will be described and compared with the measured values in Table XIV.

1. Bass Model

Bass has developed a classical model for the calculation of fusion excitation functions with a radial nuclear potential that depends on the difference in surface energies between a given finite separation and infinite separation.[74,75] This nuclear potential is written:

$$V_n(R_{12}) = -a_s A_1^{1/3} A_2^{1/3} \frac{d}{R_1+R_2} \exp\left(-\frac{R_{12}-(R_1+R_2)}{d}\right) \quad (18)$$

where a_s = 17 MeV is the surface energy coefficient in the liquid drop

mass formula,[92] d = 1.35 fm is the surface diffuseness, and $R_i = 1.07\ A_i^{1/3}$ fm. Explicit formulae for the ℓ_{crit} values as a function of energy were not given but rather a graphic analysis is necessary.[74] However, Namboodiri et al. have written an analytical function for the Bass model ℓ_{crit}[93] which is written as:

$$\ell_{crit}\hbar = \left[2\mu R_{12}^2\left(E_{CM} - \frac{Z_1Z_2e^2}{R_{12}} + \frac{da_sA_1^{1/3}A_2^{1/3}}{R_{12}}\right)\right]^{1/2} \qquad (19)$$

where the parameters a_s and R_{12} retain the same meaning as in equation (18).

2. Critical Distance Model

Glas and Mosel have postulated that a critical distance of approach determines the complete fusion cross section rather than a critical ℓ value.[94,95] This approach to the calculation of complete fusion cross sections has also been discussed extensively by Lefort.[83,81] In this formulation the σ_{CF} is given by the expression:

$$\sigma_{CF} = \left(\frac{\hbar\omega I_B}{2\mu E}\right) \text{In}\ \frac{1 + \exp[2\pi(E-V_B)/\hbar\omega}{1 + \exp[2\pi(E-V_B-I_{CR}(E-V_{CR})/I_B\hbar\omega]} \qquad (20)$$

where I_B, V_B are the moment of inertia and potential energy at the interaction distance (R_B), while I_{CR} and V_{CR} are the same quantities at the critical distance (R_{CR}). E is the center of mass energy and $\hbar\omega$ is the barrier curvature. Based on the analysis of a large amount of data Lefort and coworkers have found that:[83,96]

$$R_{CR} = (1.0 \pm .07)(A_1^{1/3} + A_2^{1/3})\ \text{fm} \qquad (21)$$

Ngo has found that the values of V_{CR} are given by:[97]

$$V_{CR} = (0.124275\ Z_1Z_2 - 17.6)\ \text{MeV}\ ,\quad Z_1Z_2 < 1000 \qquad (22)$$

$$V_{CR} = (0.11705\ Z_1Z_2 - 6.9)\ \text{MeV}\ ,\quad Z_1Z_2 > 1000 \qquad (23)$$

The values contained in Table XIV were calculated with Equations 20-23 using $R_B = 1.44(A_1^{1/3} + A_2^{1/3})$fm and $\hbar\omega = 5$ MeV. As remarked by Scobel et al. this approach should be valid if $Z_1Z_2 < 1700$,[21] that is, for all the systems in this study. The value of ℓ_{crit} was obtained as:

$$\ell_{crit}\,\hbar = \left[\frac{\sigma_{CF}}{\pi\lambda^2}\right]^{\frac{1}{2}} \qquad (24)$$

This employs the sharp cutoff model and the approximation that $\sum_{0}^{\ell_{CR}} (2\ell + 1) = \ell_{CR}^{\ 2}$.

As can be seen in Table XIV both models are in reasonable agreement with the experimental data that had been previously reported.[28,85] However, as the projectile mass increases (reaction asymmetry decreases) the models predict too large a cross section, or too large a value for the critical ℓ value.

TABLE XIV. Comparison of ℓ_{crit} with Theoretical Calculations.

System	E_{CMS} (MeV)	ℓ_{crit}^{exp} (ħ)	ℓ_{crit} Bass Model (ħ)	ℓ_{crit} Critical Distance (ħ)	Reference
$^{12}C+^{197}Au$	119	53 ± 8	55.8	52.6	Natowitz, 85
$^{40}+^{165}Ho$	181	86 ± 5	80.1	75.2	Hanappe, et al., 28
$^{48}Ca+^{159}Tb$	217	82 ± 8	109.5	107.9	this work
$^{56}Fe+^{140}Ce$	243	34 ± 5	109.5	93.1	this work

V. CONCLUSIONS

Several conclusions can be drawn from this work. The first one is that a radiochemical, nee radioanalytic, study of the complete fusion process can provide useful information on the gross features of the process. These types of study have the tremendous advantage of requiring only a very small amount of accelerator time and can be very important in uncovering the reaction mechanisms operating as new preliminary heavy ion beams become available.

A second conclusion is that rather sharp changes in the complete fusion reaction are taking place as the projectile ion enters the first row of the transition metal region of the periodic table. It had been known that large changes had occurred between ^{40}Ar induced reactions and ^{84}Kr induced reactions and a clue was obtained for ^{56}Fe + U by Reus et al. that things were changing r· ·.[16] However, the Reus study suffered from the problem that the co nucleus was unknown and predicted to be unstable.[92] These studi.s and comparisons with previous studies of the complete fusion reaction to produce At compound nuclei indicate that the fusion of projectiles heavier than ^{40}Ar with medium mass targets is severely restricted.

A third conclusion is that current models of the heavy ion induced complete fusion process are unable to predict the sharp decline in σ_{CF} that has been observed.

Finally, this work indicates that there is indeed a very large and unexpected effect of entrance channel on the reaction mechanisms, showing up particularly in the Ar - Fe region. This should have serious

consequences for studies such as those of Oganessian who has apparently not seen this effect.[98] This can also be taken as a refutation of the comment of R. Stock that "just creeping up 16 nucleous from Ar cannot make any difference to reaction mechanisms."[99] Although to be fair, this comment was directed at relativistic heavy ion reactions, it does point out the startling nature of the demise of complete fusion.

REFERENCES

1. Nuclear Spectroscopy and Reactions, Part B, J. Cerny, ed. Academic Press, New York (1974).

2. J.R. Huizenga, Nuklonika 20, 1 (1975).

3. J.R. Huizenga, Acct. Chem. Res. 9, 325 (1976).

4. A. Ghiorso, J.M. Nitschke, J.R. Alonso, C.T. Alonso, M. Nurmia, G.T. Seaborg, E.K. Hulet and R.W. Lougheed, Phys. Rev. Lett. 33, 1490 (1974).

5. T.D. Thomas, Ann. Rev. Nucl. Sci. 18, 343 (1968).

6. T. Sikkeland, Ark. Fys. 36, 539 (1967); Phys. Lett. 27B, 277 (1968).

7. M. Lefort, C. Ngo, J. Peter and B. Tamain, Nucl. Phys. A216, 166 (1973).

8. K.L. Wolf, J.P. Unik, J.R. Huizenga, J. Birkeland, H. Freiesben, and V.E. Viola, Phys. Rev. Lett. 33, 1105 (1974).

9. J.V. Kratz, A.E. Norris and G.T. Seaborg, Phys. Rev. Lett. 33, 502 (1974).

10. W.U. Schröder and J.R. Huizenga, Annal. Rev. Nucl. Sci. 27, (1977).

11. R.J. Otto, M.M. Fowler, D. Lee and G.T. Seaborg, Phys. Rev. Lett. 36, 135 (1976).

12. R. Vandenbosch, M.P. Webb, T.D. Thomas and M.S. Zisman, Nucl. Phys. A263, 1 (1976).

13. C.E. Bemis, Jr. and J.R. Nix, Comment. Nucl. Part. Phys. 7, 65, (1977).

14. Proceedings of the Symposium on the Macroscopic Features of Heavy Ion Collisions, Argonne National Laboratory Report ANL/PHY-76-2, 1976, Vol. I: Invited Papers and Vol II: Contributed Papers.

15. Proceedings of the European Conference on Nuclear Physics with Heavy Ions, Caen 1976. J. de Phys. Colloque No. 5, C-5 (1976).

16. U. Reus, A.M.H. Wätzig, R.A. Esterlund, P. Patzett and I.S. Grant, Phys. Rev. Lett. 39, 171 (1977).

17. J. Peter, Institut de Physique Nucléaire Report - IPNO-RC-75-08, 1975.

18. J.V. Kratz, J.O. Liljenzin, A.E. Norris and G.T. Seaborg, Phys.

Rev. C13, 2347 (1976).

19. G.J. Mathews, G.J. Wozniak, R.P. Schmitt, and L.G. Moretto, Z. Physik A283, 247 (1977).

20. H.H. Gutbrod, W.G. Winn and M. Blann, Phys. Rev. Lett. 30, 1259 (1973).

21. H.H. Gutbrod, W.G. Winn and M. Blann, Nucl. Phys. A213, 267 (1973).

22. W. Scobel, H.H. Gutbrod, M. Blann and A. Mignerey, Phys. Rev. C14, 1808 (1976).

23. M.N. Namboodiri, E.T. Chulick, J.B. Natowitz and R.A. Kenefick, Phys. Rev. C11, 401 (1975).

24. H.C. Britt, B.H. Erkkila, R.H. Stokes, H.H. Gutbrod, F. Plasil, R.L. Ferguson and M. Blann, Phys. Rev. C13, 1483 (1976).

25. J. Péter, C. Ngo, and B. Tamain, Nucl. Phys. A250, 351 (1975).

26. J. Bisplinghoff, P. David, M. Blann, W. Scobel, T. Mayer-Kuckek, J. Ernst and A. Mignerey, Phys. Rev. C17, 177 (1978).

27. C.M. Lederer, Table of the Isotopes, 7th Ed., private communication (1978).

28. B. Tamain, C. Ngo, J. Peter and F. Hanappe, Nucl. Phys. A252, 187 (1975).

29. G.L. Trigg, Systematics of Stable Nuclei, in D.W. Gray (ed.), AIP Handbook. 2nd ed. McGraw-Hill, New York, 1963.

30. A.H. Wapstra and K. Bos, Atomic Nucl. Data Tables 17, 474 (1976).

31. W.D. Myers, Atomic Nucl. Data Tables 17, 411 (1976).

32. See, for example, A. deShalit and H. Feshback, Theoretical Nuclear Physics, J. Wiley and Sons, New York, 1974, p. 56.

33. J.O. Rasmussen and K. Sugawara-Tanabe, Nucl. Phys. A171, 497 (1971).

34. C.Y. Wong, Phys. Rev. Lett. 31, 766 (1973).

35. See, for example, L. Kavalski, J.C. Jordogne and J.M. Miller, Phys. Rev. 169, 894 (1968).

36. See, for example, H. Gauvin, D. Guerreau, Y. LeBeyec, M. Lefort, F. Plasil and X. Tarrago, Phys. Lett. 58B, 163 (1975).

37. M. Hille, P. Hille, H.H. Gutbrod and M. Blann, Nucl. Phys. A252,

496 (1975).

38. R.L. Fleischer, P.B. Price and R.M. Walker, Nuclear Tracks in Solids; Principles and Applications, Univ. of Calif. Press, Berkeley, 1975.

39. F. Hanappe, M. Lefort, C. Ngo, J. Peter and B. Tamain, Phys. Rev. Lett. 32, 738 (1974).

40. J.V. Kratz, H. Ahrens, W. Bögl, W. Brüschle, G. Franz, M. Schadel, I. Warnecke, G. Wirth, G. Klein and M. Weis, Phys. Rev. Lett. 39, 984 (1977).

41. W. Loveland, R.J. Otto, D.J. Morrissey and G.T. Seaborg, Phys. Rev. Lett. 39, 320 (1977).

42. D.J. Morrissey, R.J. Otto, D. Lee, J.O. Liljenzin, I. Binder, M.M. Fowler, W. Loveland and G.T. Seaborg, Proceedings of the ANS Conference on Computers in Activation Analysis and Gamma-Ray Spectroscopy, Mayaguez, 1978, and Lawrence Berkeley Laboratory Report LBL-7199 (1978).

43. D. Lee, R.J. Otto, D.J. Morrissey and G.T. Seaborg, Lawrence Berkeley Laboratory Report LBL-7711 (1978), submitted for publication in Nucl. Inst. Meth. (1978).

44. I. Binder, Ph.D. Thesis, Univ. of Calif., Berkeley (1977), and Lawrence Berkeley Laboratory Report LBL-6526 (1977).

45. D.C. Hoffman and M.M. Hoffman, Annl. Rev. Nucl. Sci. 24, 151 (1974).

46. H.A. Grunder and F.B. Selph, Proceedings of the 1976 Proton Linear Accelerator Conference, Chalk River, 1976, and Lawrence Berkeley Laboratory Report LBL-5390, (1976).

47. R.J. Otto, D.J. Morrissey, D. Lee, A. Ghiorso, J.M. Nitschke, G.T. Seaborg, M.M. Fowler and R.J. Silva, J. Inorg. Nucl. Chem., in press (1978).

48. D.J. Morrissey, W. Loveland, R.J. Otto and G.T. Seaborg, Phys. Lett., 74B, 35 (1978).

49. J.M. Nitschke, R.E. Leber, M.J. Nurmia, and A. Ghiorso, Lawrence Berkeley Laboratory Report, LBL-6534 Rev (1978), submitted for publication in Nucl. Phys. A (1978).

50. E.K. Hulet, R.W. Lougheed, J.F. Wild, J.H. Landrum, P.C. Stevenson, A. Ghiorso, J.M. Nitschke, R.J. Otto, D.J. Morrissey, P.A. Baisden, B.F. Gavin, D. Lee, R.J. Silva, M.M. Fowler, and G.T. Seaborg, Phys. Rev. Lett. 39, 385 (1977).

51. B.F. Gavin, IEEE Transactions on Nucl. Sci. NS-23, 1008 (1976).

52. R.D. Giaugue, private communication, 1977.

53. A. Ghiorso, private communication, 1976.

54. B.V. Jarrett and J.D. Meng, private communication, 1975.

55. J.T. Routti and S.G. Prussin, Nucl. Inst. Meth. 72, 125 (1969).

56. J.T. Routti, Lawrence Berkeley Laboratory Report, UCRL-19452 (1969), unpublished.

57. M.M. Fowler, private communication, 1975.

58. A.T. Hirshfeld, D.D. Hoppes, and F.J. Schima, Proceedings of the X and Gamma Ray Symposium, Ann Arbor, 1976, p. 90.

59. I. Binder, R. Kraus, R. Klein, D. Lee and M.M. Fowler, Lawrence Berkeley Laboratory Report LBL-6515 (1977), unpublished.

60. W.W. Bowman and K.W. MacMurdo, Atomic Data and Nuclear Data Tables, 13, 89 (1974).

61. R.D. Evans, The Atomic Nucleus, McGraw-Hill, New York (1955), p. 484.

62. L.C. Northcliffe and R.F. Schilling, Nuclear Data Tables, 7, 233 (1970).

63. K. Guttner, S. Hofmann, D. Marx, G. Munzenberg and F. Nickel, Nucl. Inst. Meth. 146, 413 (1977).

64. A.C. Wahl. Proceedings of the Symposium on the Physics and Chemistry of Fission, Salzberg, 1965, Vol. I, 317.

65. See, for example, C.M. Lederer, J.M. Hollander and I. Perlman, Table of Isotopes, 6th, J. Wiley, New York, 1967.

66. R.J. Otto, private communication, 1975.

67. L.C. Moretto, J. Sventek and G. Mathews, Bul. Am. Phys. Soc. 23, 522 (1978), and private communication, 1978.

68. T.D. Thomas, Phys. Rev. 116, 703 (1959).

69. J.R. Huizenga and G. Igo, Nucl. Phys. 29, 462 (1961).

70. L.C. Vaz and J.M. Alexander, Phys. Rev. C10, 464 (1974).

71. H.J. Krappe, Proceedings of the Symposium on Classical and Quantum Mechanical Aspects of Heavy Ion Collisions, Heidelberg, 1974, p. 24,

and references therein.

72. W.D. Myers, Nucl. Phys. A204, 386 (1973).

73. J. Blocki, J. Randrup, W.J. Swiatecki, and C.F. Tsang, Annl. Phys. 105, 427 (1977).

74. R. Bass, Nucl. Phys. A231, 45 (1974).

75. R. Bass, Phys. Lett. 47B, 139 (1973).

76. The term "dynamite factor" has been coined to describe the ratio of the calculated mass yield to the observed radionuclide cross section.

77. J.P. Bondorf, F. Dickman, D.H.E. Gross and P.J. Siemens, J. de Phys. C6, 145 (1971).

78. C. Toepfler, J. de Phys. C6, 291 (1971).

79. See, for example, L.G. Moretto and R. Schmitt, J. de Phys. C5, 109 (1976).

80. L.G. Moretto and J.S. Sventek, Proceedings of the Symposium on the Macroscopic Features of Heavy Ion Collisions, Argonne National Laboratory Report ANL/PHY-76-2, p. 235 (1976).

81. M. Lefort, Proceedings of the Symposium on Classical and Quantum Mechanical Aspects of Heavy Ion Collisions, Heidelberg, 1974, p. 274.

82. M. Lefort, Rep. Prog. Phys. 39, 129 (1976).

83. M. Lefort, J. de Phys. C5, 57 (1976).

84. L. Kowalski, J.C. Jodogne and J.M. Miller, Phys. Rev. 169, 894 (1968).

85. See, for example, J.B. Natowitz, Phys. Rev. C1, 623 (1969).

86. R.P. Schmitt, private communication, 1978.

87. W.E. Frahn, Annl. Phys. 72, 524 (1972), and references therein.

88. J.S. Blair, Phys. Rev. 108, 827 (1975), and references therein.

89. E. Rutherford, Phil. Mag. 21, 669 (1911).

90. A.M. Zebelman and J.M. Miller, Phys. Rev. Lett. 30, 27 (1973).

91. J.R. Birkelund, J.R. Huizenga, J.N. De and D. Sperber, Phys. Rev. Lett. 40, 1123 (1978).

92. W.D. Myers and W.J. Swiatecki, Nucl. Phys. 81, 1 (1966).

93. M.N. Namboodiri, E.T. Chulick, J.B. Natowitz and R.A. Kenefick, Phys. Rev. C11, 401 (1975).

94. D. Glas and U. Mosel, Nucl. Phys. A237, 429 (1975).

95. D. Glas and U. Mosel, Phys. Rev. C10, 2620 (1974).

96. J. Galin, D. Guerreau, M. Lefort and X. Tarrago, Phys. Rev. C9, 1018 (1974).

97. C. Ngo, Ph.D. Thesis, Universite Paris-Sud, 1975.

98. Yu. Ts. Oganessian, Proceedings of the Symposium on the Classical and Quantum Mechanical Aspects of Heavy Ion Collisions, Heidelberg, 1974, p. 221.

99. R. Stock, comment made at the BEVALAC PAC meeting, Spring, 1978 on the difference between ^{40}Ar and ^{56}Fe.

FIGURE CAPTIONS

(1) The final charge dispersion curve for "fission" products from the $^{48}Ca + ^{159}Tb$ reaction. Shown are the measured yields (solid points) and the independent yields corrected for precursor decay on the basis of the fitted Gaussian curve (open points).

(2) Mass dispersion curves for products in the near-projectile region for the ^{56}Fe + Ce system. Note that maximum values of the isotopic curves fall by a factor of 10 in 6 Z units. The data points have been corrected for precursor decay on the basis of the fitted isobaric yield curves.

(3) The mass distribution curve ($\frac{d\sigma}{dA}$ vs. A) for the ^{48}Ca + Ce system. The area under the curves has been normalized to the mean geometrical cross section (see text). Macroscopic reaction channel components to the mass distribution curve are labeled: A - evaporation residue products, B - complete fusion-fission products, C and D - light and heavy deep inelastic transfer products, respectively, and E and F - light and heavy quasielastic transfer products.

(4) The mass distribution curve for the $^{48}Ca + ^{159}Tb$ system, normalized similar to Figure 3 (see text).

(5) The mass distribution curve for ^{56}Fe with Ce. Note the lack of evaporation residues and the predominance of quasi elastic transfer products.

(6) The mass distribution curve for ^{56}Fe with Tb; note the similarity to Figure 5.

(7) A schematic representation of the ℓ dependence of the reaction channels in heavy ion reactions.[86]

(8) The critical angular momenta for fusion as a function of projectile Z to form an At compound nucleus, this work plus references 28 and 85. Also shown are the maximum entrance channel angular momenta (solid squares).

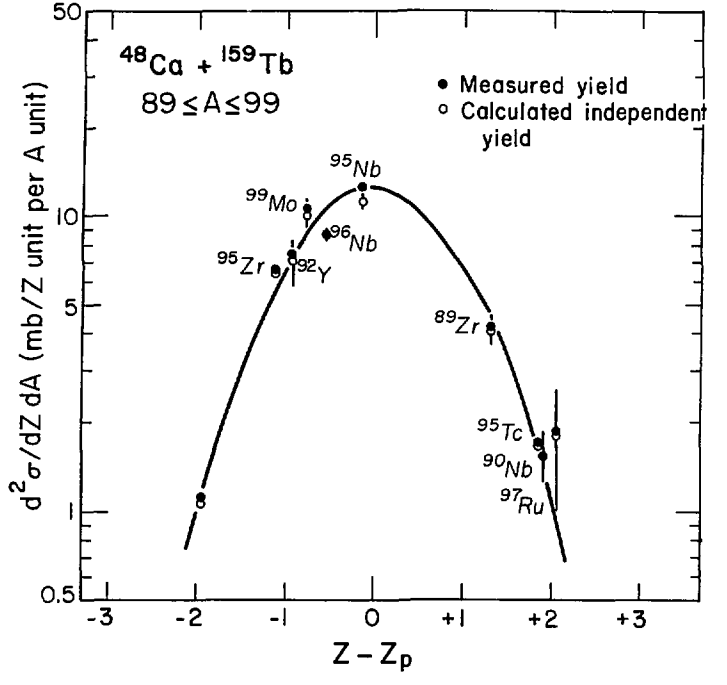

XBL 785-810

Fig. 1

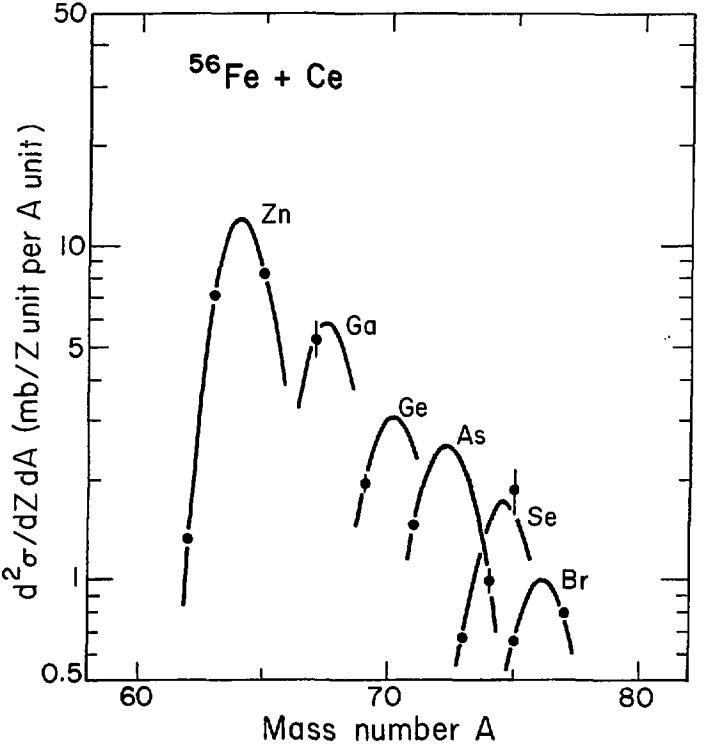

XBL 785-808

Fig. 2

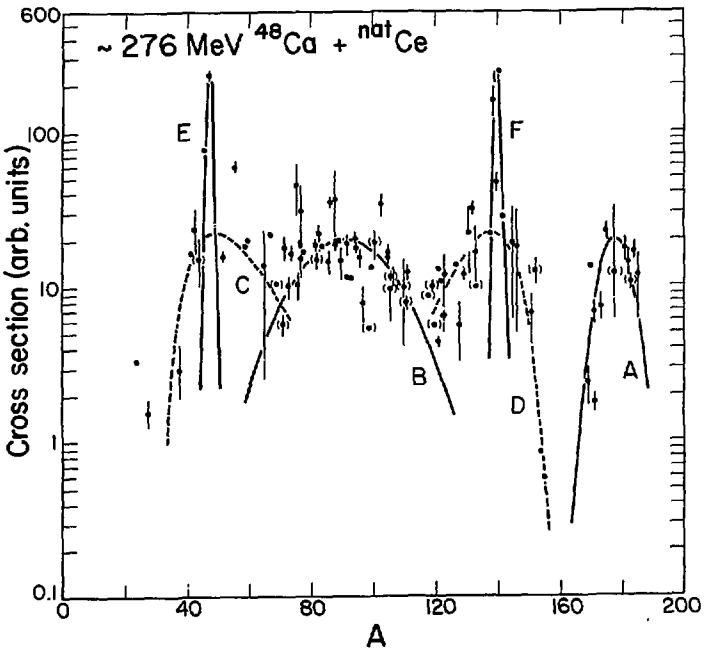
~ 276 MeV 48Ca + natCe
Cross section (arb. units)
600
100
10
1
0.1
0
40
80
120
160
200
A
E
C
B
F
D
A
XBL 778-1700

Fig. 3

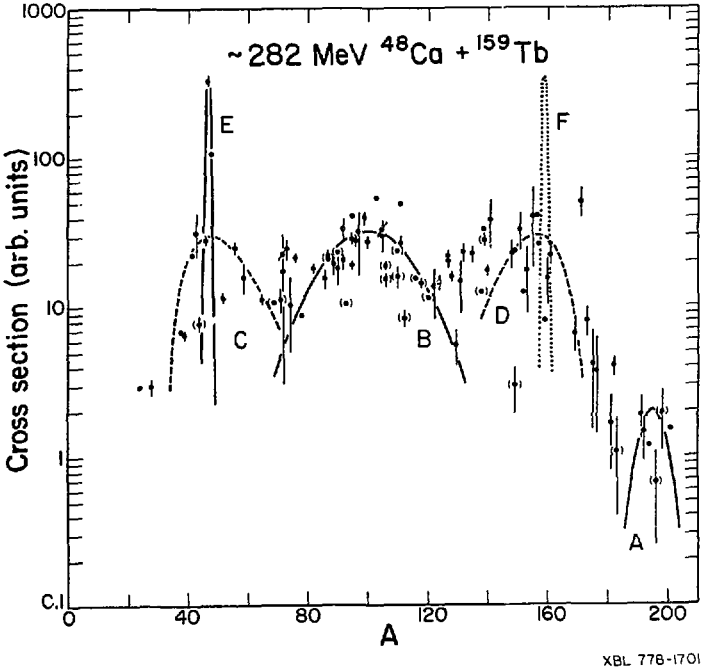
~282 MeV 48Ca + 159Tb
Cross section (arb. units)
1000
100
10
1
C.I
0
40
80
120
160
200
A
E
F
C
B
D
A
XBL 778-1701

Fig. 4

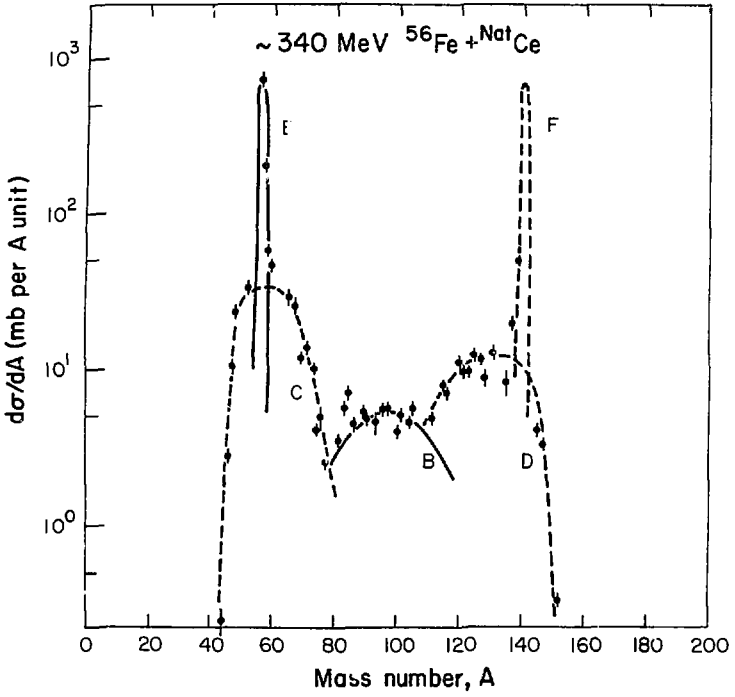

XBL 785-811

Fig. 5

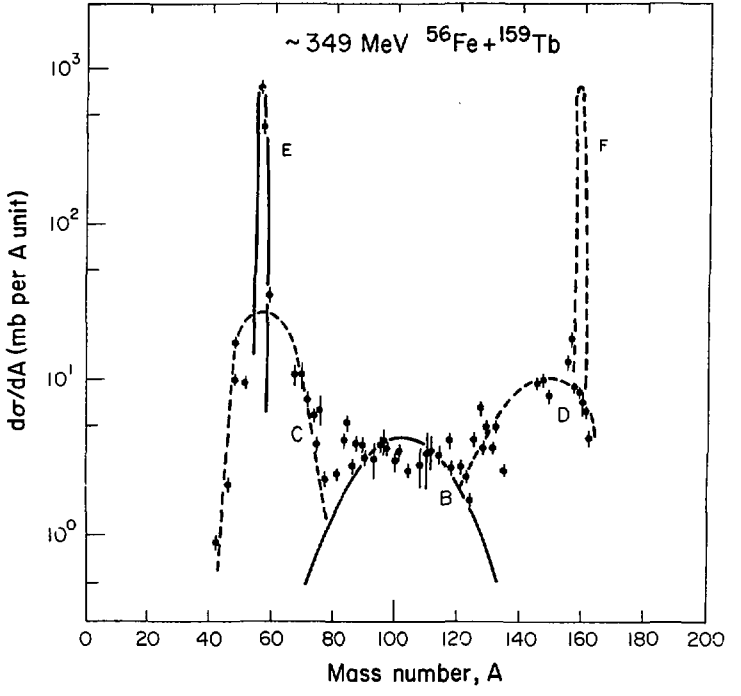

XBL 785-812

Fig. 6

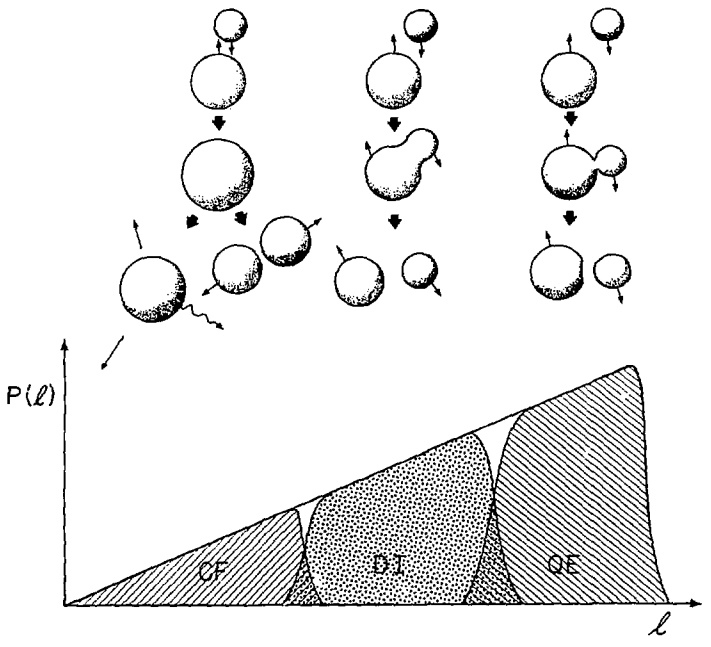

XBL 784-2482

Fig. 7